Volume 59
Number 47
14 June 2023
Pages 7115–7290

ChemComm

Chemical Communications

rsc.li/chemcomm

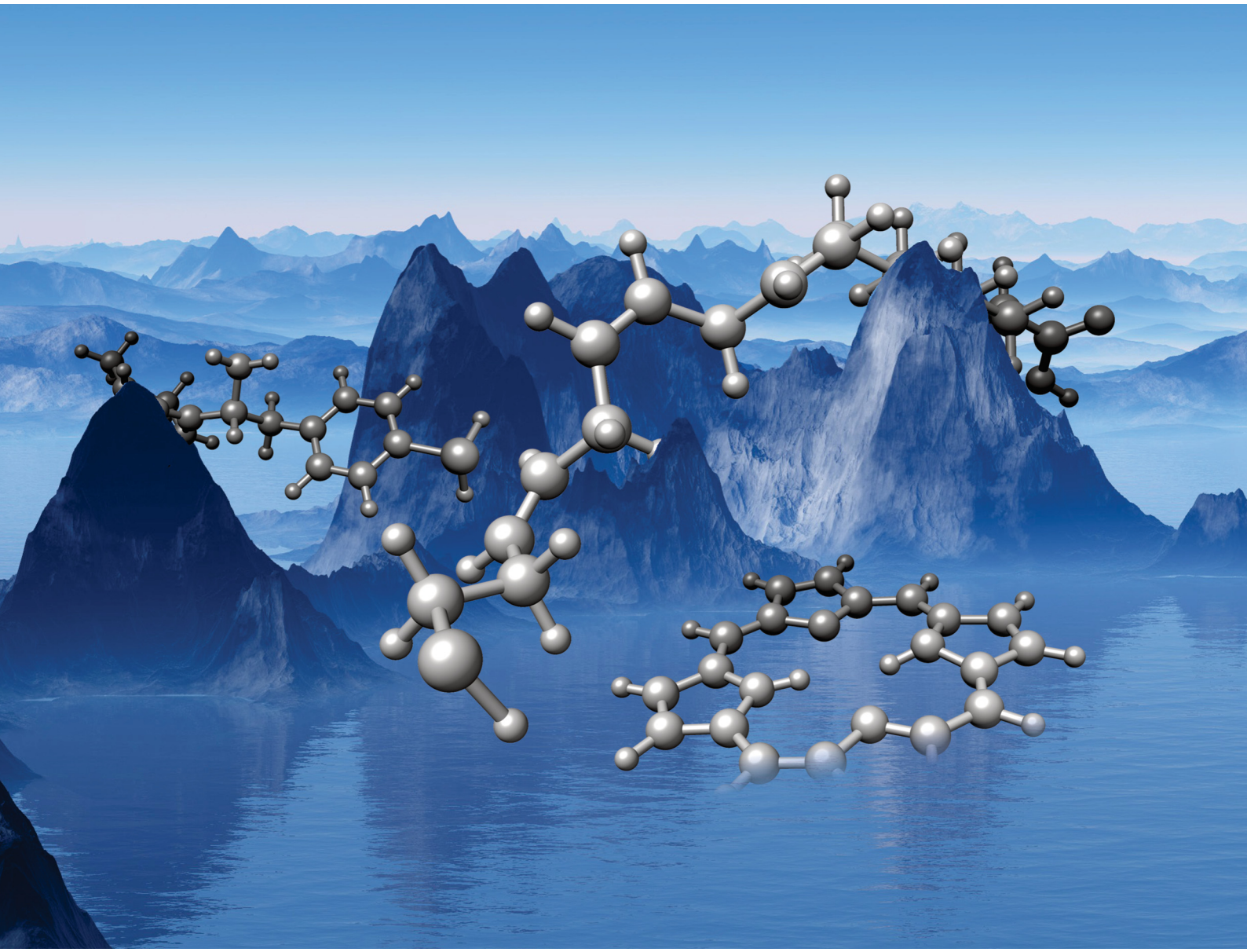

ISSN 1359-7345

ROYAL SOCIETY OF CHEMISTRY

FEATURE ARTICLE

Elfi Kraka *et al.*

Reaction mechanism – explored with the unified reaction valley approach

ChemComm

FEATURE ARTICLE

Check for updates

Cite this: *Chem. Commun.*, 2023, **59**, 7151

Reaction mechanism – explored with the unified reaction valley approach

Elfi Kraka,* Juliana J. Antonio and Marek Freindorf

One of the ultimate goals of chemistry is to understand and manipulate chemical reactions, which implies the ability to monitor the reaction and its underlying mechanism at an atomic scale. In this article, we introduce the Unified Reaction Valley Approach (URVA) as a tool for elucidating reaction mechanisms, complementing existing computational procedures. URVA combines the concept of the potential energy surface with vibrational spectroscopy and describes a chemical reaction *via* the reaction path and the surrounding reaction valley traced out by the reacting species on the potential energy surface on their way from the entrance to the exit channel, where the products are located. The key feature of URVA is the focus on the curving of the reaction path. Moving along the reaction path, any electronic structure change of the reacting species is registered by a change in the normal vibrational modes spanning the reaction valley and their coupling with the path, which recovers the curvature of the reaction path. This leads to a unique curvature profile for each chemical reaction, with curvature minima reflecting minimal change and curvature maxima indicating the location of important chemical events such as bond breaking/formation, charge polarization and transfer, rehybridization, *etc.* A decomposition of the path curvature into internal coordinate components or other coordinates of relevance for the reaction under consideration, provides comprehensive insight into the origin of the chemical changes taking place. After giving an overview of current experimental and computational efforts to gain insight into the mechanism of a chemical reaction and presenting the theoretical background of URVA, we illustrate how URVA works for three diverse processes, (i) [1,3] hydrogen transfer reactions; (ii) α-keto-amino inhibitor for SARS-CoV-2 M^{pro}; (iii) Rh-catalyzed cyanation. We hope that this article will inspire our computational colleagues to add URVA to their repertoire and will serve as an incubator for new reaction mechanisms to be studied in collaboration with our experimental experts in the field.

Received 31st March 2023,
Accepted 15th May 2023

DOI: 10.1039/d3cc01576a

rsc.li/chemcomm

1 Introduction

Chemistry plays an important role in guaranteeing the sustainability of our world, both with regard to renewable energy, the economical use of natural resources, the generation of new materials with desirable properties, the control and preservation of our environment, or the unraveling of the chemistry of life. All these tasks require that chemists are able of controlling chemical reactions, which in turn implies the understanding of the mechanism of chemical reactions to the extent that new reactions can be designed on the drawing board without too many trial and error attempts at the bench. The optimization of reaction yields must become a rational design approach and the prevention of toxic products must be part of the design process of a reaction rather than an emergency measure after the fact.

Computational and Theoretical Chemistry Group (CATCO), Department of Chemistry, Southern Methodist University, 3215 Daniel Ave, Dallas, TX 75275-0314, USA. E-mail: ekraka@gmail.com

Starting with the law of conservation of mass discovered by Lavoisier in 1789, chemists across the disciplines have tried to explore why and how chemical reactions occur and which molecular properties to measure for this purpose. Valuable overall insights into chemical reactions can be obtained from measured and/or computed kinetic data such as reaction rates or yields, or thermo-physical data including thermodynamic and transport properties.[1–3] The efficiency and accuracy of experimental instrumentation and computer hardware/software have improved significantly over time, offering today data with increasing accuracy, often collected in large databases,[4,5] along with improved statistical methodologies and advanced software packages for data analysis.[6–8] Also artificial intelligence (AI) has entered the scene, where algorithms learn to create and predict reaction outcomes, such as reaction rates, intermediates, products, and yields.[9–15] AI has been utilized to design, discover, and explore new chemical reactions, *e.g. via* deep generative recurrent neural networks,[16] or the design of 7 000 000 new reactions utilizing a variational autoencoder (VAE).[17]

This journal is © The Royal Society of Chemistry 2023

Whereas kinetic and thermo-physical data provide valuable information about the feasibility of a chemical reaction, and assessment of the performance of a catalyst in lowering the activation enthalpy, which are important factors for large scale production in chemical industry, these macroscopic properties do not necessarily disclose the intrinsic mechanism happening at the atomistic level. However, this ultimately needs to be known to fine-tune chemical reactions, improve the efficiency and turnover number of catalysts, and to systematically derive new design principles and protocols.

A promising way to move into this direction are so-called *in situ*/*operando* techniques[18] including *in situ* electron paramagnetic resonance spectroscopy (EPR),[19] sum frequency generation vibrational spectroscopy,[20] Raman spectroscopy,[21] absorption near edge structure (XANES) spectroscopy and K-edge extended X-ray absorption fine structure (EXAFS) spectroscopy,[22,23] X-ray powder diffraction (XRPD)[24–26] or synchrotron and neutron scattering-based techniques,[27] complemented with computational efforts,[7] just to name a few. These techniques collect data about the chemical reaction as it proceeds. Another technique that has a significant impact in materials science is the scanning tunneling microscope (STM), which can visualize the movement of molecules while they are involved in a chemical reaction at the surface.[28,29] A long debated question if one can observe a transition state (TS) of a chemical reaction was pioneered by Neuwark and shown through Zewail's work which won the 1999 Nobel Prize in Chemistry. It is important to note that the definition of a TS can be broad.[30] Zewail was able to elucidate apparent TS structures, with femtosecond spectroscopy experiments.[31–33] Field and collaborators have also had success in finding TSs of isomerization reactions with photodissociation spectroscopy.[34,35] Utilizing single-molecule spectroscopy in combination with fluorescence and force measurements have been applied to measure transition path times for protein folding.[36–38] Although experimental *in situ*/*operando* techniques have made a huge step forward over the past decade, there are still some limitations to overcome, such as time resolution. In this situation computational chemistry offers a helping hand complementing the experimental data and exploring possibilities for improvement of current reactions and the design of reaction pathways. For example, quantum chemical calculations have been able to 'see' conventional transition states through theoretical spectroscopy in converged quantum mechanical calculations of the energies and lifetimes of the energy levels.[39]

The concept of the potential energy surface (PES) forms the fundamental basis of almost all computational accounts on

Elfi Kraka

Elfi Kraka is Full Professor and Chair of the Department of Chemistry at Southern Methodist University, Dallas, Texas, USA since 2009 and since 2017 head of the Computational and Theoretical Chemistry group (CATCO). She received her Dr rer. nat. in Theoretical Chemistry at the University of Cologne, Germany with summa cum laude. CATCO's research mission is to develop modern quantum chemical tools and apply these tools to solve pending problems in chemistry, biology, materials science, and beyond. Current research topics stretch from catalysis, vibrational spectroscopy to machine learning supported computer assisted drug design. She has published more than 250 peer-refereed articles and presented her research at about 150 international conferences. She is a member of the Scientific Board of the World Association of Theoretical and Computational Chemists (WATOC) and serves on several Editorial Boards.

Juliana J. Antonio

Juliana Antonio attended the University of Texas at Rio Grande Valley where she received her BSc with honors in chemistry. She is currently a 1st year PhD student in the CATCO research group at Southern Methodist University. Her current research interests include QM/MM of organometallic proteins with vibrational local mode analysis and reaction mechanism profiles of various organometallic complexes. She is the recipient of an SMU Mustang PhD fellowship.

Marek Freindorf

Marek Freindorf graduated with MS and PhD (with honors) in Chemistry and minor in Physics from Jagiellonian University (Poland) in 1988. He was a faculty member in Chemistry Department of Jagellonian University till 2000 and worked as a postdoctoral research associate in University of Bonn (Germany), University at Buffalo NY (USA), and University of Louisville KY (USA). From 2011 he works in Chemistry Department of SMU (USA) currently holding a Research Professor position. He has authored more than 60 papers involving theoretical molecular spectroscopy, computations of homogeneous catalysis with transition metals, and QM/MM calculations of DNA and protein active sites.

This journal is © The Royal Society of Chemistry 2023

chemical reaction mechanisms, as well as major parts of theoretical molecular spectroscopy.[40–42] The PES is the mathematical relationship between the potential energy of the reaction complex (RC, the union of reacting species) and its geometry. Under the consideration of the Born–Oppenheimer approximation, which states that in a molecule the nuclei are essentially stationary compared to the electrons, a point on the PES, *i.e.*, the potential energy of the RC for set of fixed nuclear positions, can be obtained by a standard electronic structure calculation. For a RC being composed of N atoms, mapping the PES spanned by the N_{vib} dimensional space, with $N_{vib} = 3N - N_{tr}$, where N_{tr} describes translations and rotations ($N_{tr} = 5$ for a linear and $N_{tr} = 6$ for a non-linear RC) is a formidable task, because the total number of sampling points is $M^{(N_{vib})}$, where M is the number of points taken for each degree of freedom. In particular, if a model chemistry is applied for the electronic structure calculation aiming towards chemical accuracy, computational resources are quickly exhausted even for smaller systems, demanding for clever strategies including machine learning and AI.[9,43–50]

Fortunately, not all locations on the PES are of importance for a chemical reaction, such as the high energy regions. The often pursued poor man's approach is to exploit the reaction *via* the analysis of the stationary points, *i.e.*, reactant (R) and product (P) minima and the enclosed saddle point of first order (TS). There are various strategies (*i.e.*, geometry optimization routines) for locating these points without resorting to mapping the full PESs,[51–57] with TS searches being more difficult,[58–60] requesting often chemical intuition and/or resorting to empirical rules, such as the Hammond–Leffer postulates[61,62] as well as to AI.[63–65] After locating the stationary points, their identification as minima and/or TS, is mandatory by a subsequent frequency calculation, a routine procedure in standard quantum chemistry packages. Depending on the model chemistry used, reaction enthalpies and barriers can be obtained from the stationary points with chemical accuracy (*i.e.*, with errors smaller than one kcal mol^{-1}).[1] Analyzing the optimized geometries and molecular properties, such as charges, dipole moments, frequencies, *etc.* at R, P, and TS, also provides some qualitative insight into the reaction mechanism.

For more complex reaction systems, a subsequent reaction path (RP) calculation needs to clarify if the stationary points under consideration are connected by the same RP. A variety of procedures are available to calculate the RP being traced out by the RC on its way from an entrance to exit channel[66–73] including algorithms for automatically finding RPs[71,74–77] and methods for working in a reduced dimensional space.[78] One of the most popular reaction path is the so-called intrinsic reaction coordinate (IRC) path.[79–81] Other alternatives include nudged elastic band[82,83] or growing string-Newton trajectory paths, which can be useful for reactions without a barrier.[84] Once the RP is determined further insight into the reaction mechanism can be obtained by collecting and analyzing molecular properties of the RC along the RP. Some representative examples include (i) monitoring changes of the topological features of the electron density[85,86] or the electron localization function[87] along the RP[88–90]; (ii) the reaction force and force constant method, which is aimed at extracting information from higher derivatives of the energy profile taken along the RP,[91–93] where one has to take into account that the energy is a cumulative property and as such the mechanistic information obtained is more of a holistic nature; (iii) the discussion of local reactivity descriptors, *e.g.*, the Fukui function, and how they infer reactivity trends along the RP[94,95]; and (iv) the recently suggested exploration of the PES with immersive virtual reality.[96]

A complementary approach of monitoring the reaction mechanism is pursued in *ab initio* molecular dynamics (MD) simulations as to provide an atomic visualization into the detail of molecular reactions on a femtosecond time scale.[97–100] MD simulations can be performed on a previously constructed PES or alternatively with a direct methodology calculating the trajectories on the fly.[101–103] In contrast to classical MD which relies on Newton's equation, *ab initio* MD is based on the Schrödinger equation. It offers a more realistic simulation of complex molecular systems and processes from first principles.[104,105] MD has also been connected with machine learning procedures.[15,106,107]

The Unified Reaction Valley Approach (URVA), developed in our group[108–113] offers another complementary way to monitor the progress of a chemical reaction, namely *via* an in-depth analysis of the RP and its vicinity, forming together the so-called reaction valley, which is described in the following section.

2 The unified reaction valley approach

URVA combines the concept of the PES with vibrational spectroscopy. The progress of a chemical reaction from reactants *via* TS to products is described by a large amplitude vibrational mode, defining the movement along the RP and the remaining $(N_{vib} - 1)$ vibrational modes perpendicular to the path are used to define the surrounding reaction valley. The idea of describing a reacting system *via* a large amplitude motion and perpendicular vibrational modes goes back to the early work of Hofacker,[114] Hougen,[115] Marcus,[116–118] Levine, Duff, Truhlar, and Kupperman[79,119–121] and was further elaborated by Miller, Handy, and Adams (MHA) in their seminal work on the reaction path Hamiltonian (RPH).[122] Impressive independent work on this topic was published by Kato and Morokuma in the same year.[123]

The RPH is a classical Hamiltonian, describing the RC *via* a one-dimensional reaction parameter s, (*i.e.*, the arc length of the RP) and conjugated momentum p_s and a set of normal coordinates Q_μ and conjugated momenta P_μ (with $\mu = 2,\ldots,N_{vib}$)

$$H[s,p_s,Q_\mu,P_\mu] = T[s,p_s,Q_\mu,P_\mu] + V(s,Q_\mu) \quad (1)$$

The potential $V[s,Q_\mu]$ is approximated at each path point s by the potential $V_0(s)$ along the path plus the potential for harmonic displacements perpendicular to the path

$$V[s,Q_\mu] = V_0(s) + \frac{1}{2}\sum_{\mu=2}^{N_{vib}} \left(k_\mu^g\right)^2(s) {Q_\mu}^2(s) \quad (2)$$

The kinetic energy $T[s,p_s,Q_\mu,P_\mu]$ is composed of the momentum p_s along the RP and the momenta P_v orthogonal to the path

direction as well as so-called coupling terms $B_{\mu s}(s)$ and $B_{\mu\nu}(s)$

$$T\left[s, p_s, Q_\mu, P_\mu\right] = \frac{1}{2}\frac{\left[p_s - \sum_{\mu,\nu=2}^{N_{vib}} B_{\mu\nu}(s)Q_\mu(s)P_\nu(s)\right]^2}{\left[1 + \sum_{\mu,\nu=2}^{N_{vib}} B_{\mu\nu}(s)Q_\mu(s)\right]^2} \quad (3)$$

The $B_{\mu\nu}(s)$ terms describe the coupling between the $(N_{\text{vib}} - 1)$ vibrational modes perpendicular to the path along s. Since this motion can be considered as a rotation of the transverse vibrational modes, they are often referred to as Coriolis couplings. They are given by the dot product between the generalized mass weighted normal mode vector $\tilde{\ell}^g_\mu(s)$ and the change of the normal mode vector $\tilde{\ell}^g_\nu(s)$ with regard to s and *vice versa*:[122]

$$B_{\mu\nu}(s) = \tilde{\ell}^g_\nu(s)^\dagger \frac{\mathrm{d}\tilde{\ell}^g_\mu(s)}{\mathrm{d}s} = -B_{\nu\mu}(s) \quad (4)$$

The $B_{\mu s}(s)$ terms reflect the coupling between the vibrational modes μ perpendicular to the RP and the large amplitude motion along the RP.

The RP is a curved line in N_{vib} dimensional space. As such, its direction and curvature can be derived with the Frenet–Serret formalism,[124] as depicted in Fig. 1. The RP direction at a path point s is given by the unit vector $\eta(s)$:

$$\eta(s) = \frac{\mathrm{d}\tilde{\mathbf{x}}(s)}{\mathrm{d}s} = -\frac{\tilde{\mathbf{g}}(\tilde{\mathbf{x}}(s))}{\|\tilde{\mathbf{g}}(\tilde{\mathbf{x}}(s))\|} \quad (5)$$

where the derivative of the mass-weighted reaction coordinate $\tilde{\mathbf{x}}(s)$ with regards to s is equal to the normalized mass-weighted gradient vector $\tilde{\mathbf{g}}(s) \equiv \tilde{\mathbf{g}}(\tilde{\mathbf{x}}(s)) = \mathbf{M}^{1/2}\mathbf{g}(s)$ and $\mathbf{M}$ is a diagonal matrix of atomic masses. The curvature vector $\kappa(s)$ is given by:[108,125]

$$\begin{aligned}\kappa(s) &= \frac{\mathrm{d}^2\tilde{\mathbf{x}}(s)}{\mathrm{d}s^2} = \frac{\mathrm{d}\eta(s)}{\mathrm{d}s} \\ &= \frac{-1}{\|\tilde{\mathbf{g}}(s)\|}\left(\tilde{\mathbf{f}}^x(s)\eta(s) - \left[(\eta(s))^\dagger\tilde{\mathbf{f}}^x(s)\right]\eta(s)\right)\end{aligned} \quad (6)$$

One of the key findings of MHA's RPH work,[122] serving as the platform for URVA, is the connection between the $B_{\mu s}(s)$ terms and the reaction path curvature $\kappa(s)$, as reflected in the definition of the $B_{\mu s}(s)$ as the dot product between the reaction path vector $\eta(s)$ and the change of the normal vector $\tilde{\ell}^g_\mu(s)$ equivalent to the dot product of $\tilde{\ell}^g_\mu(s)$ and the change of $\eta(s)$ with regard to s, which corresponds to the reaction path curvature $\kappa(s)$

$$B_{\mu s}(s) = \eta(s)^\dagger \frac{\mathrm{d}\tilde{\ell}^g_\mu(s)}{\mathrm{d}s} = -\tilde{\ell}^g_\mu(s)^\dagger \frac{\mathrm{d}\eta_\mu(s)}{\mathrm{d}s} = \tilde{\ell}^g_\mu(s)^\dagger \kappa(s) \quad (7)$$

leading to

$$\kappa(s) = [\kappa(s)\kappa(s)]^{\frac{1}{2}} = \left[\sum_{\mu=2}^{N_{\text{vib}}} {B_{\mu s}}^2(s)\right]^{\frac{1}{2}} \quad (8)$$

Due to this relationship, the $B_{\mu s}$ coefficients are called curvature couplings.

The main focus of the RPH was and still is to be used as a tool for the calculation of the dynamics of a chemical reaction, and in particular, the calculation of rate constants and tunneling coefficients;[126–128] or as a valuable resource for laser spectroscopists working in the field of vibrationally driven reactions, which includes enhancement of reaction rates, manipulation of energy disposal, and promotion of a certain product channel by mode selective excitation.[129–133] However, the depth of mechanistic information provided by the RPH was not fully exploited in a systematic way, until Kraka, Cremer, and co-workers started to transform the RPH approach into an advanced mechanistic tool, coined as the Unified Reaction Valley approach URVA.[108–110,134]

2.1 Reaction path curvature and chemical change

As depicted in Fig. 2, similar to valley paths in a mounting range, reaction paths on a PES are curved rather than straight lines, which forms a key feature of URVA.

During the course of a chemical reaction, the RC changes its electronic structure. This is directly registered by the vibrational modes, which are sensitive to even the smallest electronic structure changes. The change in the vibrations leads to a change in the coupling between valley and path motions as is described by $B_{\mu s}(s)$ coefficients, which altogether define the scalar reaction path curvature, as shown in eqn (8). Therefore, URVA's main focus is on the scalar curvature $\kappa(s)$.

Monitoring the $\kappa(s)$ along s leads to a unique curvature profile for each chemical reaction, with curvature maxima K and minima M as schematically shown in Fig. 3. The curvature maxima define the locations of electronic structure change such as charge transfer, polarization, rehybridization, bond cleavage/formation, or change in the optimal orientation of the reactants for reactive collision. Curvature minima M are locations of minimal change, reflecting the transition from one chemical event to the next. Often they are the location of so-called hidden intermediates[135–137] which may transform into a real intermediate upon changed reaction conditions and/or changing the electronic environment. Tantillo describes the not true minima(s) as 'frustrated non-intermediates'.[138] There are also perspectives on full hidden intermediates that are not detected by IRC-based methods (this is different from partially or explicit hidden intermediates that are on the 'shoulders' of the IRC path).[139] It is interesting to note that these full hidden intermediates are only reachable through molecular dynamics

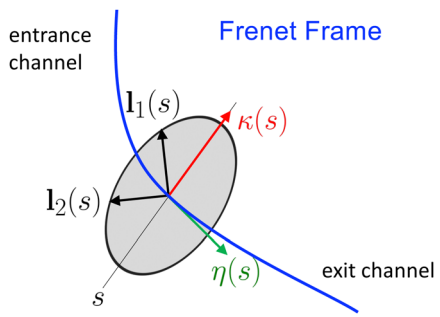

Fig. 1 Path direction and curvature of a multidimensional path described with a Frenet–Serret frame.

 This journal is © The Royal Society of Chemistry 2023

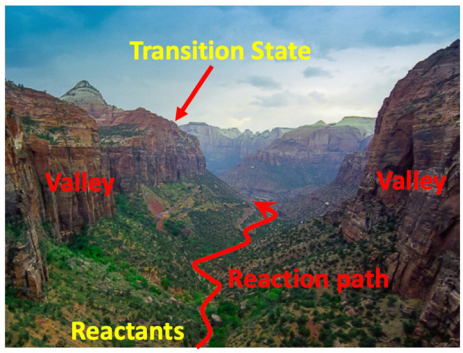

Fig. 2 Illustration of reaction path and surrounding valley on a PES *via* a real mountain range.

or 'hot' trajectories.[140,141] As revealed by Fig. 3 each curvature peak is flanked by two curvature minima. This allows to split up a chemical reaction into meaningful chemical *r*eaction phases.[109,111,113] Different chemical reactions are characterized by different curvature patterns with varying numbers of reaction phases, which reflects their signature, *i.e.*, the fingerprint of the reaction.

2.2 Decomposition of reaction path curvature

Further specific insights into the reaction mechanism, *i.e.*, the disclosure of what chemical event is happening in a specific reaction phase, require a decomposition of $\kappa(s)$ into components (red, blue, orange and purple lines in Fig. 3). The sign of the component denotes whether it supports the chemical change (positive sign) or resists it (negative sign). Typically, only a few components at a given path position s contribute to the curving of the reaction path, which allows for the analysis of larger chemical reactions more feasible.[108,137,142–147]

Originally, the decomposition of $\kappa(s)$ into $B_{\mu s}(s)$ coefficients was performed, following the MHA's RPH protocol.[109,122,130,133,148] However, it turned out that such a decomposition, while it gives

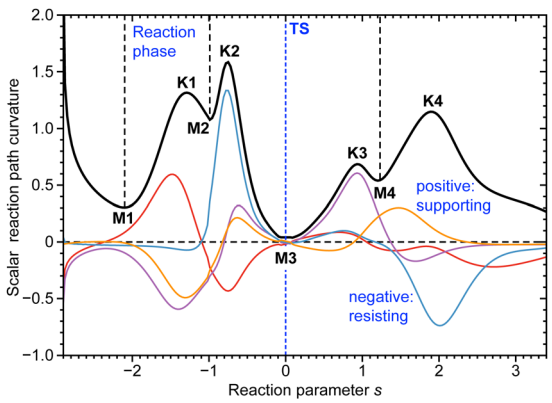

Fig. 3 Schematic representation of the scalar curvature $||\kappa(s)||$ (black solid line) given as a function of the reaction parameter s for a model reaction. Curvature minima *M* and curvature maxima *K* are shown. The location of the TS is denoted by a dotted blue line. Reaction phases are denoted by dashed black lines. Four curvature components are shown in blue, red, orange and purple.

important information for laser enhancement of reaction rates or energy decomposition into vibrational modes,[109] is of limited use for the decoding of the actual reaction mechanism, in particular in the case of larger systems, since the $B_{\mu s}(s)$ are based on normal vibrational modes (see eqn (8)). Another problem from utilizing this protocol often leads to unphysical frequencies, which can be solved with curvilinear internal coordinates to obtain physical frequencies.[149,150] As already pointed out by Wilson in 1941,[151,152] normal vibrational modes often tend to delocalize over larger parts of a molecule, and in this way disguise the actual mechanism. Therefore, Konkoli, Cremer, and Kraka suggested to decompose $\kappa(s)$ into local curvature coupling coefficients A_{ns}^{κ} based on local vibrational modes $\mathbf{a}_n$ that are associated with the internal coordinates $q_n(s)$ (with $n = 1,...N_{\text{vib}}$) used to describe the RC; the first milestone of URVA.[108,109] The local vibration mode theory has been recently described in two comprehensive review articles.[153,154] The local curvature coupling coefficients A_{ns}^{κ} are defined as[108,109]

$$A_{ns}^{\kappa} = \kappa(s)^{\dagger} \frac{\mathbf{a}_n^g}{\|\mathbf{a}_n^g(s)\|} \tag{9}$$

The curvature decomposition into local modes $\mathbf{a}_n^g(s)$ *via* eqn (9) has been successfully applied to a number of organic reactions in our group (for examples, see Table 1). However, it fails in the case of path instabilities (typically reflected by the occurrence of imaginary reaction valley frequencies). These path instabilities can be caused by methodological limitations (*e.g.*, in transition metal catalysis reactions or bond breaking/forming processes leading to multi-reference character) or can have a chemical origin (*e.g.*, a reaction path bifurcation of the PES). Any path instability prevents the description of electronic structure changes in terms of local mode curvature coupling coefficients A_{ns}^{κ} based on local modes $\mathbf{a}_n^g(s)$. To cure this problem the decomposition of the reaction path curvature $\kappa(s)$ in terms of internal coordinates that are geometrically-based local modes $\mathbf{u}_n$ was developed; another major milestone of URVA, thereby allowing a robust reaction path analysis which is no longer sensitive to path instabilities.[155]

For each internal coordinate q_n, a unit column vector $\mathbf{u}_n$ can be defined[153–155] through its local mass $m_n^q = G_{n,n}^{-1}$ [156,157] and Wilson's **B**-matrix formalism,[152] connecting internal coordinate q_n to the Cartesian coordinates $\mathbf{x}$ *via* $\mathbf{b}_n = \mathrm{d}q_n/\mathrm{d}\mathbf{x}$,

$$\mathbf{u}_n = \frac{\mathbf{M}^{-1/2}\mathbf{b}_n^{\dagger}}{\left\|\mathbf{M}^{-1/2}\mathbf{b}_n^{\dagger}\right\|} = G_{n,n}^{-1/2}\left(\mathbf{M}^{-1/2}\mathbf{b}_n^{\dagger}\right) \tag{10}$$

where $G_{n,n} = \left(\mathbf{b}_n\mathbf{M}^{-1}\mathbf{b}_n^{\dagger}\right)$. With the help of $\mathbf{u}_n$, eqn (5) can be rewritten in the mass-weighted internal coordinate $\tilde{q}_n = (m_n^q)^{1/2}q_n$,[155]

$$\begin{aligned}\eta_n^q(s) &= \frac{\mathrm{d}\tilde{q}_n(s)}{\mathrm{d}s} = G_{n,n}^{-1/2}\frac{\mathrm{d}q_n(s)\mathrm{d}\tilde{\mathbf{x}}(s)}{\mathrm{d}\tilde{\mathbf{x}}(s)\ \mathrm{d}s} \\ &= G_{n,n}^{-1/2}\mathbf{b}_n(s)\mathbf{M}^{-1/2}\eta(s) = \mathbf{u}_n^{\dagger}\eta(s)\end{aligned} \tag{11}$$

leading to a decomposition of the reaction path direction $\eta(s)$ into internal coordinate components. Eqn (8) may also be

Table 1 Representative overview of URVA studies

Topics	Ref.
Methodology	
Reaction path Hamiltonian	109 and 133
Reaction valleys for chemical reactions	130 and 148
Diabatic ordering of normal modes in reaction valleys	134
hidden intermediates and transition states	111
Chemical reactions and mechanism	112
Reaction path curvature decomposition into components	155
Hand-in-hand URVA and QTAIM approach	161
Organic reactions	
$CH_3 + H_2$	108
$FH + H_2C{=}CH_2$	137
1,2-H shift in Methylchlorocarbene	142
Diels–Alder reaction	143
Dissociation of methylenecyclopropene and cyclopropane	84
Methylene addition to ethene	136
Vinylidene–acetylene cycloaddition reaction	162
Hydrogenation of XH_n for group IV to group VII elements X	144
Quantification of the Hammond–Leffler postulate	61
Cycloaddition of 1,3-dipoles to acetylene	163
Ringclosure reactions of 1,2,4,6-heptatetraene derivatives	159
Cycloaddition of 1,3-dipoles to ethylene	164
Formation of CN bonds in Titan's atmosphere	165
Homogenous catalysis reactions	
Catalysis and URVA, a review	113
Hydrogen release from water with borane and alane catalysts	166
Grubbs catalysis	167
(NHC)Au(I) catalyzed hydroalkoxylation of allenes	168
BF_3-catalyzed Diels–Alder reaction	146
Sharpless epoxidation of allylic alcohols	147
β-hydride eliminations in Au(I) and Au(III) complexes	169
Au(I) assisted[3,3]-sigmatropic rearrangement of allyl acetate	170
Iridium catalyzed hydrogenation of carbon dioxide	173
Enzyme reactions	
Claisen rearrangement of chorismate	171
Isomerization of 5-androstene-3,17-dione in ketosteroid isomerase	172

written in $\tilde{q}_n$ using eqn (11)[155]

$$\frac{d^2\tilde{q}_n(s)}{ds^2} = \frac{d\eta_n^q(s)}{ds} = \frac{d}{ds}\left(\mathbf{u}_n^\dagger(s)\eta(s)\right) = \mathbf{u}_n^\dagger(s)\kappa(s) + \frac{d\mathbf{u}_n^\dagger(s)}{ds}\eta(s) \quad (12)$$

$$= \|k(s)\|\cos\beta_n(s) + \left\|\frac{d\mathbf{u}_n(s)}{ds}\right\|\cos\gamma_n(s) = \kappa_n^q(s) + \eta_n^u(s) \quad (13)$$

On the right-hand side of eqn (13) the first term is the projection of $\mathbf{u}_n(s)$ onto the curvature vector $\kappa(s)$ leading to the amplitude $||\mathbf{u}_n(s)||\cos\beta_n(s) = \cos\beta_n(s) = k_n^q(s)$, as each $\mathbf{u}_n$ is a vector unit describing the local motion driven by the internal coordinate $q_n(s)$. The amplitude is scaled by the scalar curvature $||\kappa(s)||$ corresponding to the length of the curvature vector in N_{vib} dimensional space. The mixed second-order term $\eta_n^u(s)$ is determined by the change in the direction of $\mathbf{u}_n(s)$ with s and the tangent vector. The vector derivative $d\mathbf{u}_n(s)/ds$ that is orthogonal to $\mathbf{u}_n(s)$ is projected onto vector η and therefore does not have any information on the curvature.[155] Therefore, the curvature contribution of the internal coordinate q_n is defined by the first term only, *i.e.*,

$$\kappa_n^q(s) = \mathbf{u}_n^\dagger(s) + \kappa(s) \quad (14)$$

The decomposition into other coordinates, such as the Cremer–Pople puckering coordinates,[158] is possible, provided that the corresponding Wilson **B**-matrix can be derived.[113,152,159]

The URVA software (pURVA)[160] is a standalone Python code and can be obtained upon request from the authors. For details, see ref. 113.

3 URVA applications

Table 1 gives a representative overview of URVA studies ranging from organic reactions in gas phase and solution, homogenous catalysis, to reactions taking place in enzymes. In the following we present three examples, explaining how URVA can be utilized to help elucidating the reaction mechanism.

3.1 [1,3] Hydrogen transfer reactions

The first example illustrates how URVA complements the analysis of the stationary points with mechanistic details for a selection of six intramolecular [1,3] hydrogen transfer reactions (R1)–(R6) shown in Fig. 4. It is noteworthy that both formic (HC(O)OH) and thioformic acid (HC(O)SH) have recently attracted attention because they were discovered in interstellar space.[174–176] According to DLPNO-CCSD(T)/aug-cc-pVQZ calculations, (R1) proceeds *via* a four-center TS with an activation enthalpy of 34.2 kcal mol^{-1} (see Fig. 4). The C1O2 double bond (BSO = 1.991) is transformed into a single bond (BSO = 1.157), the OH hydrogen bond (BSO = 0.937) is transferred from O3 to O2, there is also a weak hydrogen interaction with the carbonyl oxygen atom (BSO = 0.393). Substituting the hydrogen of the CH spectator bond with fluorine leads to a somewhat strengthening of both CO single and double bonds (BSO values are 1.240 and 2.062, respectively) and on the other hand leads to an increase of the weak carbonyl OH interaction (BSO = 0.407) which makes it difficult to explain the increased activation enthalpy of 39.4 kcal mol^{-1} just on bond strength arguments. The corresponding curvature diagram shown in Fig. 5(a) provides a more complete mechanistic picture. The reaction proceeds in four phases starting in phase 1 with a lengthening of the C1O2 bond (supporting, red solid line) while the formation of the new H5O2 bond is resisting (green solid line) as well as the bending of the C1O3H5 angle (red dashed line). The second phase is dominated by the supportive breakage of the H5O3 bond (purple solid line), the formation of the new OH bond assisted by the bending of the C1O2H5 framework (orange solid line). This process requires 25.6 kcal mol^{-1} compared to 11.4 kcal mol^{-1} spent in the first phase. As revealed by Fig. 5(b) reaction (R2) exhibits the same curvature diagram with one exception, in phase 1 and phase 2 there is contribution of the O2C1O3 angle (dashed blue line) leading to an energy

 This journal is © The Royal Society of Chemistry 2023

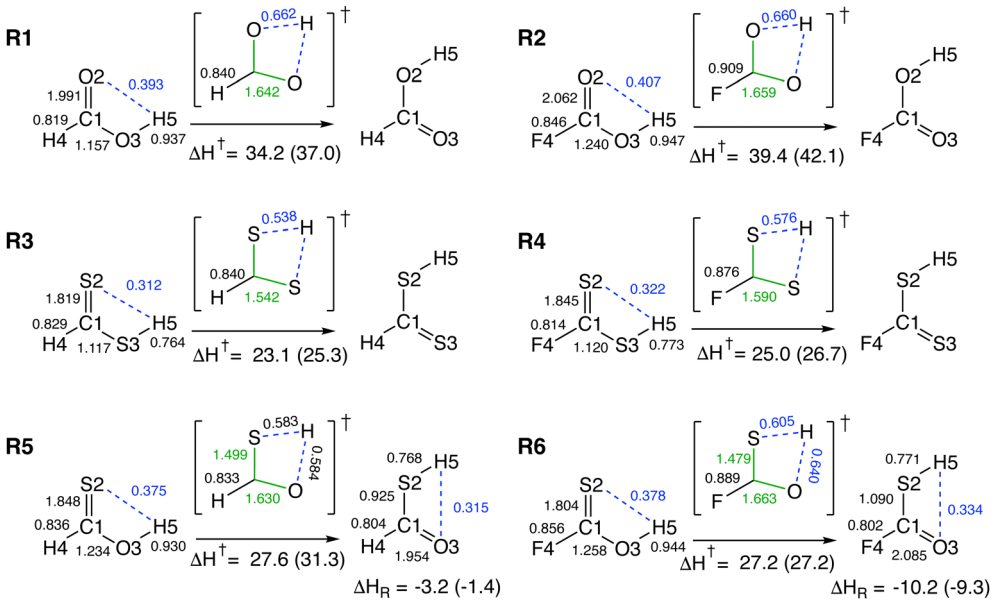

Fig. 4 [1,3] hydrogen migration reactions discussed in this section; (R1): H(O)-migration in formic acid (HC(═O)OH), (R2): H(O)-migration in fluoro formic acid (FC(═O)OH), (R3): H(S)-migration in dithioformic acid (HC(═S)SH), (R4): H(S)-migration in fluoro dithioformic acid (FC(═S)SH), (R5): H(O)-migration in thioformic acid (HC(═S)OH) (R6): H(O)-migration in fluoro thioformic acid, (FC(═S)OH). Bond strengths orders (BSO) derived from local vibrational mode force constants[153,154] calculated at the B3LYP/6-311G(d,p) level of theory[177–180] are shown. Activation enthalpies and reaction enthalpies at the DLPNO-CCSD(T)/aug-cc-pVQZ level of theory[181–183] are given (*i.e.*, DLPNO-CCSD(T)/aug-cc-pVQZ energies with thermochemical corrections from the B3LYP/6-311G(d,p) data). The corresponding B3LYP/6-311G(d,p) activation energies and reaction energies are given in parenthesis.

increase of 2.8 kcal mol^{-1} and 2.3 kcal mol^{-1} spent in phase 1 and 2 respectively.

HS-migration in dithioformic acid, reaction (R3) and in fluorodithioformic acid, reaction (R4) proceed with considerably lower activation enthalpies (23.1 and 25.0 kcal mol^{-1} respectively) compared to their formic acid counterparts as depicted in Fig. 4. Breakage of a SH bond requires less energy than breakage of a OH bond and a CS double bond is easier to transform into a CS single bond than a CO double bond, which is reflected by the reduced energy contributions to phases 2 and 1 (15.9 and 9.4 kcal mol^{-1} respectively, see Fig. 5(c)). The overall curvature patterns are the same for the formic and thioformic acid reactions. Interesting to note is that for both, reactions (R3) and (R4) the bending of the S2C1S3 plays a mechanistic role, explaining that fluorination is less influential than in the formic acid case. Reactions (R5) and (R6) show the OH migration in thioformic and fluorothioformic acid. Interesting to note is that the activation enthalpies for both reactions are almost the same (27.6 and 27.2 kcal mol^{-1}, respectively), however reaction (R6) is more exothermic (−10.2 *versus* −3.2 kcal mol^{-1}) reflecting the larger effect of fluorination at the CO than the CS bond, see Fig. 4. The corresponding curvature diagrams are shown in Fig. 5(e) and (f). As for the symmetric reactions (R1)–(R4), the H-migration proceeds in 4 phases with similar decomposition patterns, bending and CS lengthening precedes OH bond breakage. The lower peak height in phase 4 (compared with phase 1) reflects that the CSH bending potential is less stiff than the COH potential and more shallow. The higher peak in phase 2 (compared with phase 3) relates to the larger strength and stiffness of OH bonds compared to SH bonds. In summary, the mechanism in these [1,3] H-migration reactions can be seen as an interplay between both the donor/acceptor capacities of O and S atoms and the bending of the heavy atom framework, *i.e.*, according to URVA, the energy barrier will increase if the ACB (A, B = O, S) heavy atom framework is made more rigid rather than by decreasing the H-acceptor capacity of B.

3.2 α-Keto-amino inhibitors for SARS-CoV-2 M^{pro}

Beside gas phase reactions and reactions in solution, URVA can also be applied to hybrid quantum mechanics/molecular mechanics (QM/MM) methodologies.[184,185] However, one has to keep in mind that the reaction space is spanned by all QM + MM atoms (often in the range of 5000 or more) making these studies technically more challenging.[171–173] As an example our study on α-keto-amino inhibitors[186] for the main protease of SARS-CoV-2 (SARS- CoV-2 M^{pro}) is presented in the following.[187] SARS-CoV-2 M^{pro} is a cysteine protease that takes part in the viral replication process.[188–190] A recent crystal structure of the inhibitor bound to SARS-CoV-2 M^{pro}[191] suggests that α-ketoamide blocks the virus from replication *via* forming a CN bond with Cyst145 of the protease,[192–194] identifying the inhibitor as covalent binder.[195–197] Whereas weak chemical protein–drug interactions can be modeled with fast MM approaches[198] this is no longer possible when the drug forms a chemical bond with the target. Because of the direct involvement of electrons that are neglected in the MM approach a QM ansatz is required.[199,200]

The one-step formation of the CS bond between the α-ketoamide inhibitor and the side chain of Cys145 in SARS-CoV-2 M^{pro} proceeds *via* the nucleophilic attack of Cys S atom on the

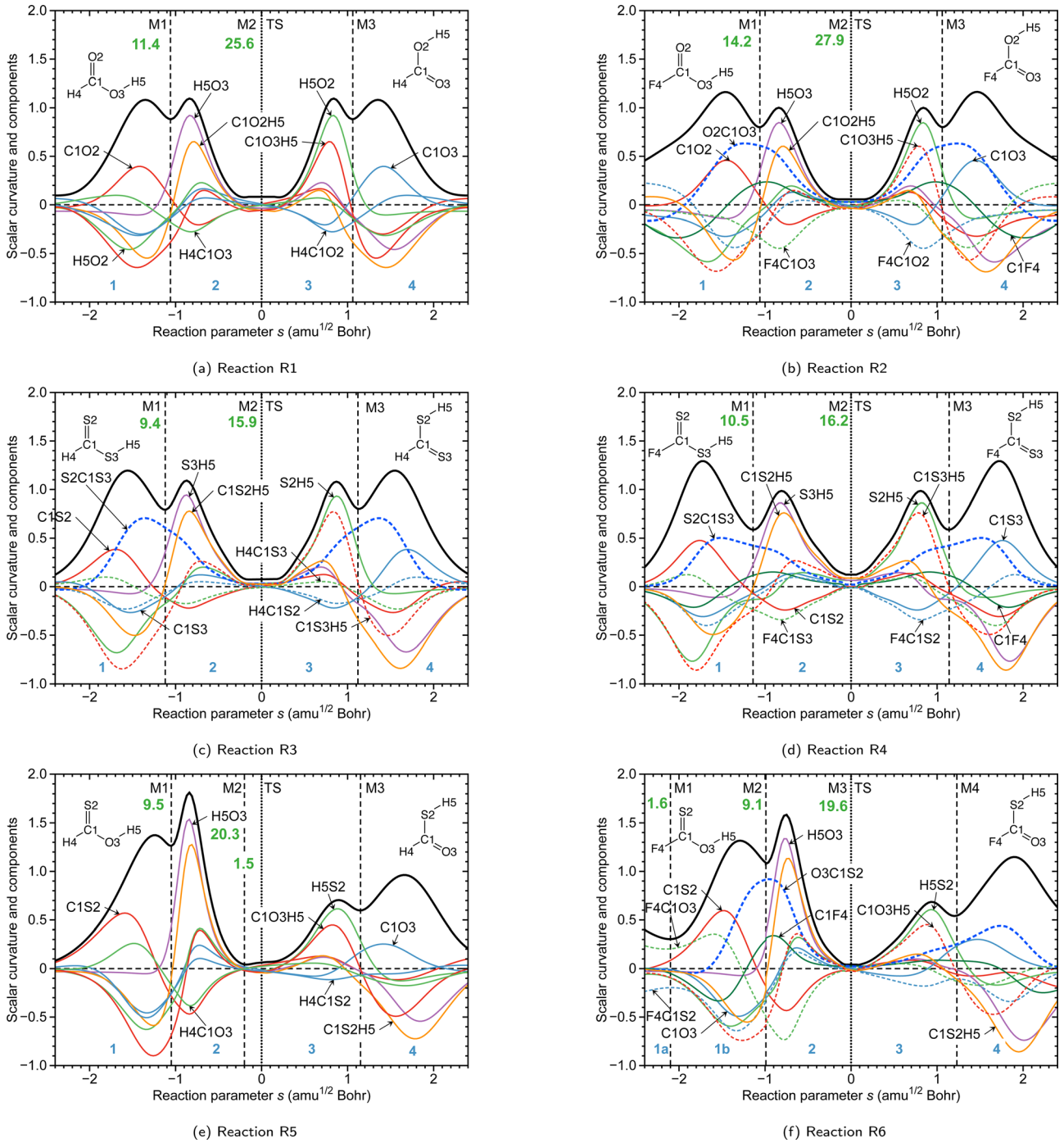

Fig. 5 Curvature profiles (black solid lines) and curvature decomposition into most important components (colored lines) for [1,3] hydrogen-migration reactions (R1)–(R6). Reaction phases defined by the curvature minima M1, M2... are indicated by dashed vertical lines and are labelled by blue numbers. The TS is indicated by a vertical dotted line. The energy contribution (in kcal mol^{-1}) from each reaction phase to the activation energy is given by the green numbers. B3LYP/6-311G(d,p) level of theory.

carbonyl C atom of the inhibitor and *via* a synchronous migration of the Cys145 HS hydrogen atom to the oxygen atom of the attacked CO bond of the inhibitor (see Fig. 6(a)). CS one-step bond formation in the protein is influenced by the interaction with the His41 residue of SARS-CoV-2 M^{pro}, which is located in close proximity of the reaction site. There are two different protonation forms of His41 determining how it interacts; in His41ε the interaction is *via* a hydrogen atom of the ε nitrogen atom of the histidine imidazole ring (Fig. 6(b)) and in His41δ *via* the lone pair of the δ nitrogen atom of the histidine imidazole ring (Fig. 6(c)). Both possibilities were considered in our QM/MM study of the protein reaction and compared with the reaction in the gas phase, where the cysteine residue was modeled by CH_3–SH.[187]

 This journal is © The Royal Society of Chemistry 2023

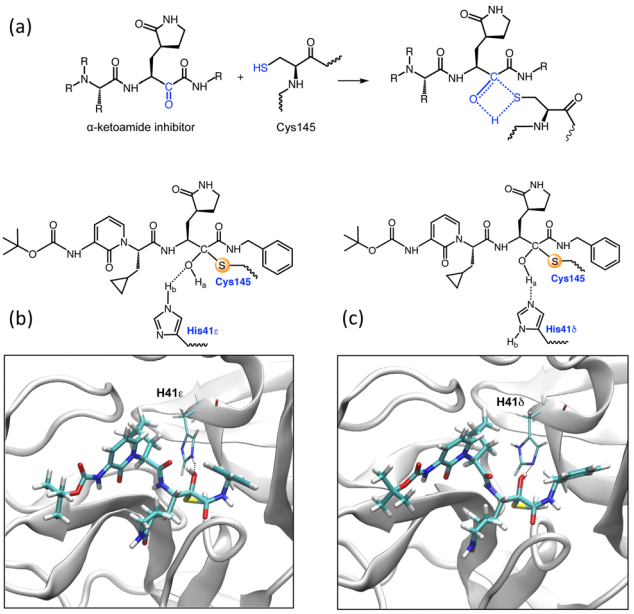

Fig. 6 (a) General one-step reaction scheme between α-ketoamide inhibitor and Cys145 of SARS-CoV-2 M^{pro}. Atoms engaged in the reaction are highlighted in blue. (b) Complex between the model α-ketoamide inhibitor used in this study and SARS-CoV-2 M^{pro}, HIS41ε form. (c) Complex between the model α-ketoamide inhibitor and SARS-CoV-2 M^{pro}, HIS41δ form. For computational details, see ref. 187.

As depicted in Fig. 7(a) the gas phase activation enthalpy of 38.4 kcal is reduced in the protein to 33.0 and 28.7 kcal mol^{-1} for the His41ε and His41δ protonation forms, respectively. This is a clear indication that the protein environment, in particular the His41 interaction, supports CS bond formation. The gas phase reaction is endothermic (ΔH_R = 8.8 kcal mol^{-1}) making it unfavorable. In contrast, the one-step reaction in the protein becomes exothermic with ΔH_R values of −3.8 and −10.6 kcal mol^{-1}, for the His41ε and His41δ protonation forms, respectively. This shows the efficiency of the inhibitor establishing a chemical bond with SARS-CoV-2 M^{pro} blocking viral replication. Whereas the energetics deliver the important proof that the inhibitor works, they cannot provide mechanistic details leading to a better understanding of what causes the decrease of the barrier in the protein and what makes the reaction exothermic in the protein environment. These questions can be tackled by URVA. Fig. 7(b) and (c) show the curvature diagrams of the three reactions.

The gas phase reaction is composed of 9 distinct reaction phases. Phases 1–4 are uneventful preparation phases which are not in Fig. 7(b). Phase 6 is characterized by the start of CS bond formation (red line) and the onset of transformation of the carbonyl CO double bond of inhibitor into a single bond (purple line), both being supportive. Hydrogen migration involving the formation of the new OH bond (green line) and the cleavage of the SH bond (blue line) are still resisting. OHS bending (dashed blue line) is strongly supporting and HSC bending is strongly resisting. Whereas OH bond formation is still resisting in phase 7, SH bond cleavage becomes supportive and dominates the large curvature peak together with COH bending (dashed red line). In phase 8 including the TS, finalization of OH bond formation becomes the dominating event accompanied by the finalization of CS bond formation as well as SH bond cleavage and CO bond adjustment leading to a large curvature peak located at the TS, *i.e.*, all these events account for the barrier. Final adjustments to the product proceeds slowly being reached at 15 path units.

As revealed by the curvature pattern shown in Fig. 7(c) and (d), the overall one-step reaction mechanism in the protein is similar to that in the gas phase, an observation we also made in previous URVA enzyme studies.[171] This also shows that even for reactions with thousands of degrees of freedom, URVA projects key reaction features into a digestible subspace, determined by the reaction phases. On the other hand URVA also discloses important differences between gas phase and protein reactions. For both the His41ε and the His41δ protonation form the large curvature peak connected with the finalization of OH bond as well as SH bond cleavage and CO bond adjustment have been moved into phase 4 after the TS which is contained in phase 3, *i.e.*, these events do not longer contribute to the energy barrier, explaining the lower activation energies in the protein. Whereas in the gas phase CS bond formation is completed synchronously with OH bond formation (see phase 8) in the protein the CS bond finalization follows OH bond finalization in phase 6. As obvious from Fig. 7(a) the protein reactions are completed faster than the gas phase reaction (9.8 and 11.5 path units for the protein reactions compared to 15 path units for gas phase reaction) which is indicative of space confinement support in the protein reaction. Interesting to note are the different curvature patterns of the His41ε and the His41δ protonation forms in the exit channel, which originate predominantly from five dihedral angles, defining the orientation of the cysteine side chain relative to the ligand (Fig. 7(c) and (d), olive line labelled as "additional"). In the His41δ protonation form these dihedral contributions form a new phase 7, where the reaction complex is moved farther along the RP on the PES, while in the His41ε they are covered by phase 6. In summary, the different exit channel curvature patterns of these two histidine forms reflect in a sensitive way the different ligand positions relative to histidine.

3.3 Rh-catalyzed cyanation

The third example concerns a homogenous catalysis topic. Cyanation, the introduction of a cyano group into an organic compound plays an important role in organic synthesis, because the cyano group can be easily transformed into functionalized products such as acid derivatives, aldehydes, amines, and heterocycles and valuable intermediates.[202–206] In general, nitriles (*i.e.*, organic compounds with a functional cyano group) have wide significance in materials science, agrochemical and pharmaceutical industry, synthesis of natural product, and pigments and dyes, just to name a few.[207–209] The first transition metal-catalyzed cyanation reaction was reported in 1919 using Cu as the catalyst.[210] Rhodium entered the scene with the discovery of Wilkonson's catalyst $[RhCl(PPh_3)_3]$[211,212] which was instrumental for the fundamental understanding of metal–H interactions and hydrogen activation leading to the

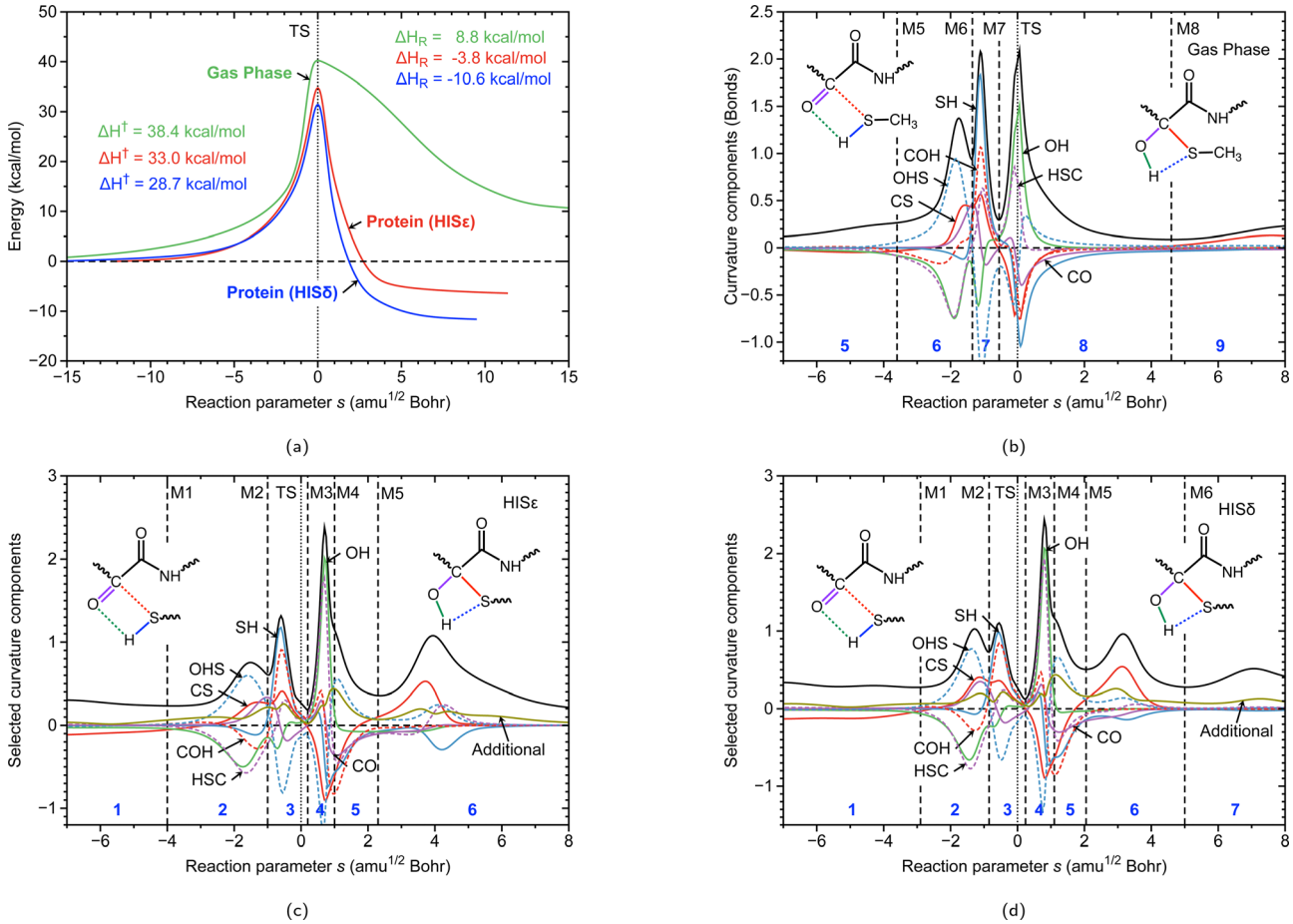

Fig. 7 (a) Reaction profiles for gas phase reaction (green color) between α-ketoamide inhibitor and CH_3–SH (simulating Cys), α-ketoamide inhibitor and Cys145 of SARS-CoV-2 M^{pro}, HISε tautomeric form (red color) as well as α-ketoamide inhibitor and Cys145 of SARS-CoV-2 M^{pro}, HISδ tautomeric form (blue color). Activation and reaction enthalpies are shown. (b) Curvature diagram for the gas phase reaction. (c) Curvature diagram for α-ketoamide inhibitor reacting with Cys145 of SARS-CoV-2 M^{pro}, HISε form. (d) Curvature diagram for α-ketoamide inhibitor reacting with Cys145 of SARS-CoV-2 M^{pro}, HISδ form. Reaction phases are between vertical dashed lines M1, M2,... and are indicated by blue numbers. The TS is indicated by a vertical dotted line. The curvature profile is given as black solid line, most important curvature components are given as solid and dashed colored lines. B3LYP/6-31G(d,p)[177–180] and B3LYP/6-31G(d,p)/AMBER[201] levels of theory in gas phase and in protein, respectively. For computational details, see ref. 187.

emerging field of designing catalysts for efficient support of both C–C bond formation and C–H cleavage *via* C–H bond activation,[213–220] and more broadly, contributing to two essential tasks in organic synthesis, namely C–C bond formation[221–224] and C–H bond activation.[225–228]

In the following we discuss the URVA results for a model reaction describing the Rh-catalyzed formation of acetonitrile starting from an $(\eta^5\text{-}C_5H_5)Rh(PH_3)(CH_3)(CN)$ complex, a simplified version of the $(\eta^5\text{-}C_5Me_5)Rh(PMe_3)(CH_3)(CN)$ catalyst suggested by Evans.[229] Following our standard URVA protocol for homogenous catalysis reactions, see *e.g.* ref. 113 we first studied the non-catalyzed model reaction between HCN and CH_4 involving both the C–C bond formation and the C–H bond cleavage, shown in Fig. 8(a) and (b). According to URVA, the reaction proceeds in 10 phases. The activation energy of 127.6 kcal mol^{-1} clearly shows that a direct reaction between alkane and HCN is without practical use. As revealed by the curvature diagram, the most expensive chemical events (phases 3 and 4) are the start of the new C–C bond formation (blue line in Fig. 8(b); supportive) and the simultaneous start of the new H–H bond formation (red line in Fig. 8(b), resisting) contributing with 53.9 kcal mol^{-1} to the activation energy and the start of C–H breakage in phase 5, (green line in Fig. 8(b), supportive) contributing with 62.7 kcal mol^{-1} to the activation energy.

Fig. 8(c) and (d) demonstrate how this is solved by the Rh catalyst, in particular how both C–C bond formation and C–H cleavage are supported in a cost effective way. The catalyst splits the reaction into two parts, a feature we have also observed for other catalysis reactions, such as the Au(I) assisted[3,3]-sigmatropic rearrangement of allyl acetate.[170] The major catalytic activities of the first reaction with a barrier 33.8 kcal mol^{-1} imply loosening of the Rh–C a bond, supporting in this way the formation of the new the C_aC_b bond, and the generation of an intermediate, which is stabilized by an agostic interaction between Rh and the C_aH_a bond. The second step, shown in

 This journal is © The Royal Society of Chemistry 2023

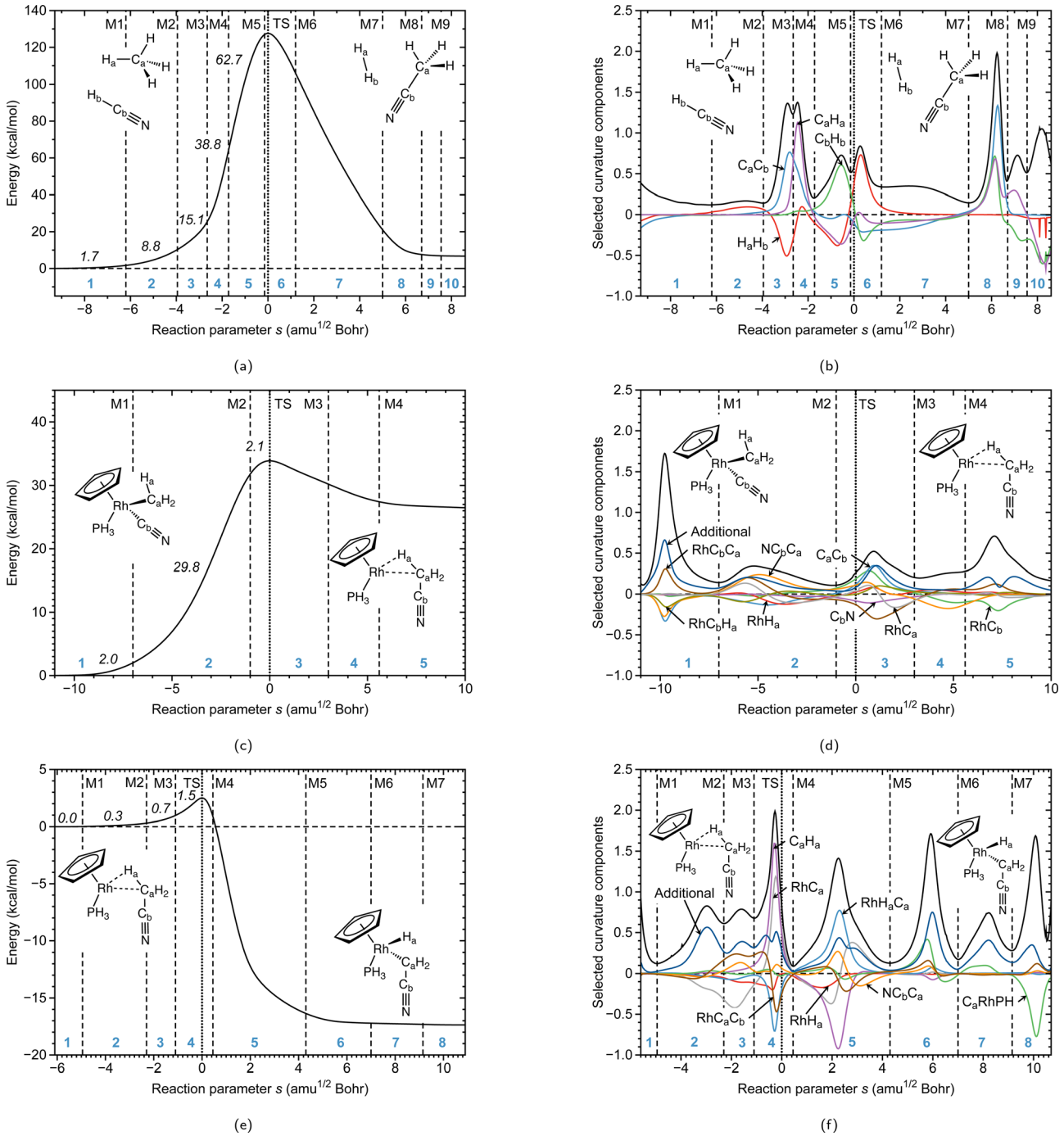

Fig. 8 Non-catalyzed model reaction (R0): CH_4 and HCN. (a) Energy profile. Energy contributions of each reaction phase to the total activation energy are shown in black italics. (b) Curvature profiles (black solid lines) and curvature decomposition into most important components (colored lines). Reaction phases defined by the curvature minima M1, M2,. . ., denoted by vertical dashed lines and labelled by blue numbers. The TS is indicated by a vertical dotted line. B3LYP/6-31G(d,p) level of theory. First step of (η^5-C_5H_5)Rh(PH_3)(CH_3)(CN) rearrangement involving C_aC_b bond formation, (R1). (c) Energy profile. (d) Curvature profile (black solid lines) and curvature decomposition into most important components (colored lines). The olive line, labelled ''additional'' accounts for the sum of 5 dihedral components, see text. Second step of (η^5-C_5H_5)Rh(PH_3)(CH_3)(CN) rearrangement involving C_aH_a bond cleavage (R2). (e) Energy profile. (f) Curvature diagram. B3LYP/6-31G(d,p) level of theory for reaction (R0), B3LYP/6-31G(d,p)/SDD(Rh)[230] level of theory for reactions (R1) and (R2).

Fig. 8(e) and (d) with a barrier of only 2.5 kcal mol^{-1} is devoted to the cleavage of the already weakened C_aH_a bond, demonstrating the perfect C–H bond activation of the catalyst. In summary this example shows how URVA provides important mechanistic details which are useful for both the fine-tuning of existing and the design of new catalysts.

4 Conclusions and future perspectives

URVA is a unique quantum chemical tool for the in-depth study of chemical reaction mechanisms at the atomic level. URVA unravels the complex interplay between the vibrations and the electronic structure changes of the RC when moving along the RP. It records all chemical events taking place from the entrance channel (van der Waals region) up to the energy pass point and then down through the exit valley to the products. Important and less-important events are differentiated by focusing on the curvature of the RP rather than analyzing features of the reaction complex itself. This makes URVA feasible also for large molecular systems with many degrees of freedom and for complex reaction mechanisms, as found in enzyme catalysis. The unique curvature profile of a chemical reaction helps find in the most efficient way the mechanistic needles in the haystack.

Three representative URVA studies are presented in this article providing a flavor of how URVA discloses the different facets of chemical reactions ranging from organic reactions in the gas phase, reactions in enzymes, to homogenous catalysis.

1. [1,3] hydrogen transfer reactions: the URVA results of the six relatively simple [1,3] hydrogen transfer reactions presented in this work disclose that the actual H-migration proceeds *via* two phases, starting with bending of the ACB framework, lengthening of the reactant C═O or C═S double bond followed by the actual H-bond migration. The overall mechanism in these reactions can be seen as an interplay between both the donor/acceptor capacities of O and S atoms and the bending of the heavy atom framework, *i.e.*, according to URVA, the energy barrier will increase if the ACB (A, B = O, S) heavy atom framework is made more rigid rather than by decreasing the H-acceptor capacity of B.

2. α-keto-amino inhibitors for SARS-CoV-2 M^{pro}: first of all it is interesting to see that the curvature diagram for an enzyme reaction with thousands of atoms is still simple and compact enough to allow the visualization of major chemical events, *i.e.*, URVA projects key reaction features into a digestible subspace, determined by the reaction phases. The overall one-step reaction mechanism in the protein is similar to that in the gas phase, an observation we also made in previous URVA enzyme studies.[171] clarifying that the enzyme does not change the overall reaction mechanism, it accelerates the reaction *via* space confinement and shifts energy consuming events into a reaction phase after the TS. Whereas in the gas phase both CS bond formation is completed synchronously with OH bond formation, in the protein the CS bond finalization follows OH bond finalization. In addition, the curvature diagram also provide subtle differences between His41ε and the His41δ complexation of the inhibitor, which are useful for fine-tuning the strength of the inhibitor-protein CS bond, blocking the replication of the virus.

3. Rh-catalyzed cyanation: this homogenous catalysis reactions illustrates our URVA roadmap for catalyst design[113,170] (i) first, study the non-catalyzed reaction; identify energy consuming events before the TS, identify hidden intermediates to be used to break up the reaction into several steps. (ii) Then identify a catalyst which can (a) transform the hidden intermediates into real intermediates and (b) change the sequence of steps and/or move the energy consuming steps into the exit channel. Overall, in non-catalyzed reactions, chemical events (*e.g.*, bond breakage/formation) often occur rather abruptly; in catalysis bond breaking may stretch over several reaction phases, thus transforming this event into an energy saving process.

URVA discloses that the unfavorably high activation energy of 127.6 kcal mol^{-1} for the non-catalyzed model reaction, *i.e.*, the direct reaction between HCN and CH_4 is caused by the fact that both CC bond formation and CH bond breakage occur before the TS. The Rh catalyst breaks up the non-catalyzed reaction into two energy saving steps. In the first step, the Rh–C a bond is loosened, supporting in this way the formation of the new the C–C bond and the generation of an intermediate, which is stabilized by an agostic interaction between Rh and the CH bond to be broken. The second almost barrier-less step is then devoted to the cleavage of the already weakened CH bond, demonstrating the perfect C–H bond activation of the catalyst. These important mechanistic details provided by URVA are useful for both the fine-tuning of existing and the design of new catalysts.

We hope that this article will inspire our computational colleagues to add URVA to their repertoire and will serve as incubator for new reaction mechanisms to be studied in collaboration with our experimental experts in the field.

Conflicts of interest

There are no conflicts to declare.

Acknowledgements

This work was financially supported by the National Science Foundation (grant CHE 2102461). We thank SMUs Center for Scientific Computing for providing generous computational resources.

Notes and references

1 K. Spiekermann, L. Pattanaik and W. H. Green, *Sci. Data*, 2022, **9**, 1–12.
2 S. Gupta, J. R. Elliott, A. Anderko, J. Crosthwaite, W. G. Chapman and C. T. Lira, *Ind. Eng. Chem. Res.*, 2023, **62**, 3394–3427.
3 A. Alibakhshi and L. V. Schäfer, Nature, *Sci. Rep.*, 2022, **12**, 5834.
4 S. M. Kearnes, M. R. Maser, M. Wleklinski, A. Kast, A. G. Doyle, S. D. Dreher, J. M. Hawkins, K. F. Jensen and C. W. Coley, *J. Am. Chem. Soc.*, 2021, **143**, 18820–18826.
5 *NIST Standard Reference Database Number 69*, ed. P. Linstrom and W. Mallard, National Institute of Standards and Technology, Gaithersburg MD, 20899, 2022.
6 H. Parastar and R. Tauler, *Angew. Chem., Int. Ed.*, 2022, **61**, e201801134.
7 S. Bhandari, S. Rangarajan and M. Mavrikakis, *Acc. Chem. Res.*, 2020, **53**, 1893–1904.
8 J. H. Thorpe, J. L. Kilburn, D. Feller, P. B. Changala, D. H. Bross, B. Ruscic and J. F. Stanton, *J. Chem. Phys.*, 2021, **155**, 184109.
9 J. Burés and I. Larrosa, *Nature*, 2023, **613**, 689–695.

 This journal is © The Royal Society of Chemistry 2023

10 P. Schwaller, A. C. Vaucher, R. Laplaza, C. Bunne, A. Krause, C. Corminboeuf and T. Laino, *Wiley Interdiscip. Rev.: Comput. Mol. Sci.*, 2022, **12**, e1604.
11 M. Meuwly, *Chem. Rev.*, 2021, **121**, 10218–10239.
12 K. Jorner, A. Tomberg, C. Bauer, C. Sköld and P.-O. Norrby, *Nat. Rev. Chem.*, 2021, **5**, 240–255.
13 M. Steiner and M. Reiher, *Top. Catal.*, 2022, **65**, 6–39.
14 T. Lewis-Atwell, P. A. Townsend and M. N. Grayson, *Wiley Interdiscip. Rev.: Comput. Mol. Sci.*, 2022, **12**, e1593.
15 F. Noé, A. Tkatchenko, K.-R. Müller and C. Clementi, *Annu. Rev. Phys. Chem.*, 2020, **71**, 361–390.
16 W. Bort, I. I. Baskin, T. Gimadiev, A. Mukanov, R. Nugamnov, P. Sidorov, G. Marcou, D. Horvath, O. Klimchuk, T. Madzhidov and A. Varnek, *Sci. Rep.*, 2021, **11**, 1–15.
17 R. Tempke and T. Musho, *Commun. Chem.*, 2022, **5**, 1–10.
18 X. Li, X. Yang, J. Zhang, Y. Huang and B. Liu, *ACS Catal.*, 2019, **9**, 2521–02531.
19 S. A. Bonke, T. Risse, A. Schnegg and A. Brückner, *Nat. Rev.*, 2021, **1**, 1–20.
20 A. Morita, *Theory of Sum Frequency Generation Spectroscopy*, Springer, Singapore, 2018.
21 M. Chen, D. Liu, L. Qiao, P. Zhou, J. Feng, K. W. Ng, Q. Liu, S. Wang and H. Pan, *Chem. Eng. J.*, 2023, **461**, 141939.
22 A. Iglesias-Juez, G. L. Chiarello, G. S. Patience and M. O. Guerrero-Pérez, *Can. J. Chem. Eng.*, 2022, **100**, 3–22.
23 *EXAFS Spectroscopy Techniques and Applications*, ed. B. K. Teo and D. C. Joy, Springer, New York, NY, 2012.
24 L. Schlicker, A. Doran, P. Schneppmüller, A. Gili, M. Czasny, S. Penner and A. Gurlo, *Rev. Sci. Instrum.*, 2018, **89**, 033904.
25 A. Doran, L. Schlicker, C. M. Beavers, S. Bhat, M. F. Bekheet and A. Gurlo, *Rev. Sci. Instrum.*, 2017, **88**, 013903.
26 R. Jenkins and R. L. Snyder, *Introduction to X-ray Powder Diffractometry*, John Wiley & Sons, Inc., New York, NY, 1996.
27 M. Hosseini, M. Arif, A. Keshavarz and S. Iglauer, *Earth-Sci. Rev.*, 2021, **221**, 103755.
28 J. A. Elemans, *Mater. Today*, 2009, **12**, 34–38.
29 D. den Boer and J. A. Elemans, *Eur. Polym. J.*, 2016, **83**, 390–406.
30 J. Bertrán, *Theor. Chem. Acc.*, 1998, **99**, 143–150.
31 P. Y. Cheng, D. Zhong and A. H. Zewail, *J. Chem. Phys.*, 1995, **103**, 5153–5156.
32 E. W.-G. Diau, S. De Feyter and A. H. Zewail, *Chem. Phys. Lett.*, 1999, **304**, 134–144.
33 C. Wan, T. Fiebig, O. Schiemann, J. K. Barton and A. H. Zewail, *Proc. Natl. Acad. Sci. U. S. A.*, 2000, **97**, 14052–14055.
34 J. H. Baraban, P. B. Changala, G. C. Mellau, J. F. Stanton, A. J. Merer and R. W. Field, *Science*, 2015, **350**, 1338–1342.
35 K. Prozument, J. H. Baraban, P. B. Changala, G. B. Park, R. G. Shaver, J. S. Muenter, S. J. Klippenstein, V. Y. Chernyak and R. W. Field, *Proc. Natl. Acad. Sci. U. S. A.*, 2020, **117**, 146–151.
36 H. S. Chung, *J. Mol. Biol.*, 2018, **430**, 409–423.
37 D. E. Makarov, A. Berezhkovskii, G. Haran and E. Pollak, *J. Phys. Chem. B*, 2022, **126**, 7966–7974.
38 N. Q. Hoffer, K. Neupane, A. G. T. Pyo and M. T. Woodside, *Proc. Natl. Acad. Sci. U. S. A.*, 2019, **116**, 8125–8130.
39 D. C. Chatfield, R. S. Friedman, D. W. Schwenke and D. G. Truhlar, *J. Phys. Chem.*, 1992, **96**, 2414–2421.
40 K. Ohno and H. Satoh, *Exploration on Quantum Chemical Potential Energy Surfaces: Towards the Discovery of New Chemistry*, The Royal Society of Chemistry, London, 2023.
41 J. Steinmetzer, S. Kupfer and S. Gräfe, *Int. J. Quantum Chem.*, 2021, **121**, e26390.
42 E. G. Lewars, *The Concept of the Potential Energy Surface*, Springer International Publishing, Cambridge, 2016, pp. 9–495.
43 H. B. Schlegel, *J. Comput. Chem.*, 2003, **24**, 1514–1527.
44 T. Takayanagi, *J. Phys. Chem. A*, 2021, **125**, 3994–4002.
45 V. V. Rybkin, *Chem. – Eur. J.*, 2020, **26**, 362–368.
46 O. T. Unke, D. Koner, S. Patra, S. Käser and M. Meuwly, *Mach. Learn.: Sci. Technol.*, 2020, **1**, 013001.
47 Y. Zhang, H. Wang, W. Chen, J. Zeng, L. Zhang, H. Wang and W. E, *Comput. Phys. Commun.*, 2020, **253**, 107206.
48 E. Quintas-Sánchez and R. Dawes, *J. Chem. Inf. Model.*, 2019, **59**, 262–271.
49 A. S. Abbott, J. M. Turney, B. Zhang, D. A. Smith, D. Altarawy and H. F. Schaefer, *J. Chem. Theory Comput.*, 2019, **15**, 4386–4398.
50 A. L. Dewyer, A. J. Argüelles and P. M. Zimmerman, *Wiley Interdiscip. Rev.: Comput. Mol. Sci.*, 2018, **8**, e1354.
51 H. B. Schlegel, *Wiley Interdiscip. Rev.: Comput. Mol. Sci.*, 2011, **1**, 790–809.
52 H. B. Schlegel, *Theor. Chem. Acc.*, 2016, **135**, 84.
53 H. P. Hratchian and H. B. Schlegel, *Theory and Applications of Computational Chemistry*, Elsevier, 2005, pp. 195–249.
54 F. Eckert, P. Pulay and H.-J. Werner, *J. Comput. Chem.*, 1997, **18**, 1473–1483.
55 R. V. de Vijver and J. Zádor, *Comput. Phys. Commun.*, 2020, **248**, 106947.
56 C. A. Grambow, L. Pattanaik and W. H. Green, *Sci. Data*, 2020, **7**, 137.
57 D. Bálint and L. Jäntschi, *Mathematics*, 2021, **9**, 2855.
58 H. Guo and K. Liu, *Chem. Sci.*, 2016, **7**, 3992–4003.
59 L. D. Jacobson, A. D. Bochevarov, M. A. Watson, T. F. Hughes, D. Rinaldo, S. Ehrlich, T. B. Steinbrecher, S. Vaitheeswaran, D. M. Philipp, M. D. Halls and R. A. Friesner, *J. Chem. Theory Comput.*, 2017, **13**, 5780–5797.
60 V. Ingman, A. Schaefer, L. Andreola and S. Wheeler, *Wiley Interdiscip. Rev.: Comput. Mol. Sci.*, 2020, e1510.
61 D. Cremer and E. Kraka, *Rev. Proc. Quim.*, 2012, 27–30.
62 G. S. Hammond, *J. Am. Chem. Soc.*, 1955, **77**, 334–338.
63 M. Z. Makós, N. Verma, E. C. Larsson, M. Freindorf and E. Kraka, *J. Chem. Phys.*, 2021, **155**, 024116.
64 P. Zheng, R. Zubatyuk, W. Wu, O. Isayev and P. O. Dral, *Nat. Commun.*, 2021, **12**, 7022.
65 P. L. Bhoorasingh, B. L. Slakman, F. S. Khanshan, J. Y. Cain and R. H. West, *J. Phys. Chem. A*, 2017, **121**, 6896–6904.
66 W. Quapp, M. Hirsch and D. Heidrich, *Theor. Chem. Acc.*, 2000, **105**, 145–155.
67 J. M. Bofill and J. M. Anglada, *Theor. Chem. Acc.*, 2001, **105**, 463–472.
68 H. B. Schlegel, *J. Comput. Chem.*, 2003, **24**, 1514–1527.
69 M. Hirsch and W. Quapp, *Chem. Phys. Lett.*, 2004, **395**, 150–156.
70 A. Aguilar-Mogas, X. Giménez and J. M. Bofill, *J. Chem. Phys.*, 2008, **128**, 104102.
71 Y. Kim, J. W. Kim, Z. Kim and W. Y. Kim, *Chem. Sci.*, 2018, **9**, 825–835.
72 A. Denzel, B. Haasdonk and J. Kästner, *J. Phys. Chem. A*, 2019, **123**, 9600–9611.
73 H. P. Hratchian and E. Kraka, *J. Chem. Theory Comput.*, 2013, **9**, 1481–1488.
74 S. Maeda, Y. Harabuchi, M. Takagi, K. Saita, K. Suzuki, T. Ichino, Y. Sumiya, K. Sugiyama and Y. Ono, *J. Comput. Chem.*, 2018, 233–250.
75 S. Maeda, Y. Harabuchi, Y. Ono, T. Taketsugu and K. Morokuma, *Int. J. Quantum Chem.*, 2015, **115**, 258–269.
76 T. Tsutsumi, Y. Ono, Z. Arai and T. Taketsugu, *J. Chem. Theory Comput.*, 2018, **14**, 4263–4270.
77 W. Quapp and J. M. Bofill, *J. Comput. Chem.*, 2020, **41**, 629–634.
78 S. R. Hare, L. A. Bratholm, D. R. Glowacki and B. K. Carpenter, *Chem. Sci.*, 2019, **10**, 9954–9968.
79 D. G. Truhlar and A. Kuppermann, *J. Am. Chem. Soc.*, 1971, **93**, 1840–1851.
80 K. Fukui, S. Kato and H. Fujimoto, *J. Am. Chem. Soc.*, 1975, **97**, 1–7.
81 K. Fukui, *Acc. Chem. Res.*, 1981, **14**, 363–368.
82 G. Henkelman and H. Jónsson, *J. Chem. Phys.*, 2000, **113**, 9978–9985.
83 V. Ásgeirsson, B. O. Birgisson, R. Bjornsson, U. Becker, F. Neese, C. Riplinger and H. Jónsson, *J. Chem. Theory Comput.*, 2021, **17**, 4929–4945.
84 W. Quapp, E. Kraka and D. Cremer, *J. Phys. Chem. A*, 2007, **111**, 11287–11293.
85 R. Bader, *Atoms in Molecules: A Quantum Theory*, Oxford University Press, 1994.
86 R. Bader, *Chem. Rev.*, 1991, **91**, 893–928.
87 A. Savin, R. Nesper, S. Wengert and T. F. Fässler, *Angew. Chem., Int. Ed. Engl.*, 1997, **36**, 1808–1832.
88 J. Andrés, L. Gracia, P. Gonzalez-Navarrete and V. Safont, *Comput. Theor. Chem.*, 2015, **1053**, 17–30.
89 J. Andrés, P. Gonzalez-Navarrete and V. S. Safont, *Int. J. Quantum Chem.*, 2014, **114**, 1239–1252.
90 V. Polo, J. Andres, S. Berski, L. R. Domingo and B. Silvi, *J. Phys. Chem. A*, 2008, **112**, 7128–7136.

91 A. Toro-Labbé, S. Gutieŕrez-Oliva, J. Murray and P. Politzer, *Mol. Phys.*, 2007, **105**, 2619–2625.
92 F. Urcelay, A. Toro-Labbé and S. Gutieŕrez-Oliva, *J. Phys. Chem. A*, 2020, **124**, 2372–2379.
93 L. Rincon, F. J. Torres, J. R. Mora, C. H. Zambrano and V. Rodriguez, *Theor. Chem. Acc.*, 2020, **139**, 313.
94 P. Geerlings, E. Chamorro, P. Chattaraj, F. De Proft, J. Gázquez, S. Liu, C. Morell, A. Toro-Labbé, A. Vela and P. Ayers, *Theor. Chem. Acc.*, 2020, **139**, 36.
95 T. Stuyver, F. D. Proft, P. Geerlings and S. Shaik, *J. Am. Chem. Soc.*, 2020, **142**, 10102–10113.
96 M. Martino, A. Salvadori, F. Lazzari, L. Paoloni, S. Nandi, G. Mancini, V. Barone and S. Rampino, *J. Comput. Chem.*, 2020, **41**, 1310–1323.
97 Z. Yang and K. N. Houk, *Chem. – Eur. J.*, 2018, **24**, 3916–3924.
98 K. Black, P. Liu, L. Xu, C. Doubleday and K. N. Houk, *Proc. Natl. Acad. Sci. U. S. A.*, 2012, **109**, 12860–12865.
99 M. Meuwly, *Wiley Interdiscip. Rev.: Comput. Mol. Sci.*, 2019, **9**, e1386.
100 J. R. Gissinger, B. D. Jensen and K. E. Wise, *Polymer*, 2017, **128**, 211–217.
101 S. Pratihar, X. Ma, Z. Homayoon, G. L. Barnes and W. L. Hase, *J. Am. Chem. Soc.*, 2017, 3570–3590.
102 M. Paranjothy, R. Sun, Y. Zhuang and W. L. Hase, *Wiley Interdiscip. Rev.: Comput. Mol. Sci.*, 2013, **3**, 296–316.
103 T. Tsutsumi, Y. Harabuchi, Y. Ono, S. Maeda and T. Taketsugu, *Phys. Chem. Chem. Phys.*, 2018, **20**, 1364–1372.
104 Y. Atalay, E. Paquet and H. L. Viktor, *Adv. Chem.*, 2018, **2018**, 9839641.
105 J. M. Bowman, G. Czakó and B. Fu, *Phys. Chem. Chem. Phys.*, 2011, **13**, 8094–8111.
106 S. Chmiela, H. Sauceda, A. Tkatchenko and K. Müller, in *Machine Learning Meets Quantum Physics, Lecture Notes in Physics*, ed. K. Schütt, S. Chmiela, O. von Lilienfeld, A. Tkatchenko, K. Tsuda and K. Müller, Springer, New York, 2020, vol. 968, pp. 129–154.
107 W. Jia, H. Wang, M. Chen, D. Lu, L. Lin, R. Car, E. Weinan and L. Zhang, Proceedings of the International Conference for High Performance Computing, Networking, Storage and Analysis, 2020, pp. 1–14.
108 Z. Konkoli, E. Kraka and D. Cremer, *J. Phys. Chem. A*, 1997, **101**, 1742–1757.
109 E. Kraka, *Wiley Interdiscip. Rev.: Comput. Mol. Sci.*, 2011, **1**, 531–556.
110 E. Kraka and D. Cremer, *Int. J. Quantum Chem.*, 2019, **119**, e25849.
111 E. Kraka and D. Cremer, *Acc. Chem. Res.*, 2010, **43**, 591–601.
112 D. Cremer and E. Kraka, *Curr. Org. Chem.*, 2010, **14**, 1524–1560.
113 E. Kraka, W. Zou, Y. Tao and M. Freindorf, *Catalysts*, 2020, **10**, 691.
114 L. Hofacker, *Z. Naturforsch., A: Astrophys., Phys. Phys. Chem.*, 1963, **18**, 607–619.
115 J. T. Hougen, P. R. Bunker and J. W. Johns, *J. Mol. Spectrosc.*, 1970, **34**, 136–172.
116 R. A. Marcus, *J. Chem. Phys.*, 1966, **45**, 4493–4499.
117 R. A. Marcus, *J. Chem. Phys.*, 1966, **45**, 4500–4504.
118 R. A. Marcus, *J. Chem. Phys.*, 1968, **49**, 2610–2616.
119 B. C. Garrett and D. G. Truhlar, *J. Am. Chem. Soc.*, 1979, **101**, 4534–4548.
120 D. G. Truhlar and D. A. Dixon, in *Atom-Molecule Collision Theory: A Guide for the Experimentalist*, ed. R. B. Bernstein, Plenum Press, New York, 1979, pp. 595–646.
121 A. D. Isaacson and D. G. Truhlar, *J. Chem. Phys.*, 1982, **76**, 1380–1391.
122 W. H. Miller, N. C. Handy and J. E. Adams, *J. Chem. Phys.*, 1980, **72**, 99–112.
123 S. Kato and K. Morokuma, *J. Chem. Phys.*, 1980, **73**, 3900–3914.
124 W. Kühnel, *Differential Geometry: Curves – Surfaces – Manifolds*, American Mathematics Society, AMS, New York, 2005.
125 M. Page and J. W. McIver, *J. Chem. Phys.*, 1988, **88**, 922–935.
126 J. L. Bao and D. G. Truhlar, *Chem. Soc. Rev.*, 2017, **46**, 7548–7596.
127 B. Garrett and D. Truhlar, in *Theory and Applications of Computational Chemistry: The First Forty Years*, ed. C. Dykstra, G. Frenking, K. Kim and G. Scuseria, Elsevier, Amsterdam, 2005, pp. 67–87.
128 J. Gonzales, X. Gimenez and J. Bofill, *Phys. Chem. Chem. Phys.*, 2002, **4**, 2921–2926.
129 D. Luckhaus, *Phys. Chem. Chem. Phys.*, 2008, **10**, 6215–6222.
130 E. Kraka and T. H. Dunning, Jr., in *Advances in Molecular Electronic Structure Theory: The Calculation and Characterization of Molecular Potential Energy Surfaces*, ed. T. H. Dunning Jr., JAI Press, Inc., Greenwich, 1990, pp.129–173.
131 T. H. Dunning Jr., E. Kraka and R. A. Eades, *Faraday Discuss. Chem. Soc.*, 1987, **84**, 427–440.
132 T. H. Dunning, Jr., L. B. Harding and E. Kraka, in *NATO Advanced Research Workshop on "Supercomputer Algorithms for Reactivity, Dynamcis and Kinetics of Small Molecules"*, ed. T. H. Dunning, Jr., Kluwer Academic Publishers, Dordrecht, Holland, 1989, p. 57.
133 E. Kraka, *Encyclopedia of Computational Chemistry*, John Wiley & Sons, New York, 1998, pp. 2437–2463.
134 Z. Konkoli, D. Cremer and E. Kraka, *J. Comput. Chem.*, 1997, **18**, 1282–1294.
135 R. Kalescky, W. Zou, E. Kraka and D. Cremer, *J. Phys. Chem. A*, 2014, **118**, 1948–1963.
136 H. Joo, E. Kraka, W. Quapp and D. Cremer, *Mol. Phys.*, 2007, **105**, 2697–2717.
137 D. Cremer, A. Wu and E. Kraka, *Phys. Chem. Chem. Phys.*, 2001, **3**, 674–687.
138 D. J. Tantillo, *J. Phys. Org. Chem.*, 2008, **21**, 561–570.
139 S. Shaik and P. Hiberty, *A Chemists Guide to Valence Bond Theory*, Wiley-Interscience, 2008.
140 T. Bekele, C. F. Christian, M. A. Lipton and D. A. Singleton, *J. Am. Chem. Soc.*, 2005, **127**, 9216–9223.
141 R. Duran, C. Barrales-Martinez and R. A. Matute, *Phys. Chem. Chem. Phys.*, 2023, **25**, 6050–6059.
142 E. Kraka and D. Cremer, *J. Phys. Org. Chem.*, 2002, **15**, 431–447.
143 E. Kraka, A. Wu and D. Cremer, *J. Phys. Chem. A*, 2003, **107**, 9008–9021.
144 E. Kraka, W. Zou, M. Freindorf and D. Cremer, *J. Chem. Theory Comput.*, 2012, **8**, 4931–4943.
145 T. Sexton, E. Kraka and D. Cremer, *J. Phys. Chem. A*, 2016, **120**, 1097–1111.
146 M. Freindorf and E. Kraka, *Catalysts*, 2022, **12**, 415.
147 M. Freindorf and E. Kraka, *Catalysts*, 2022, **12**, 789.
148 T. H. Dunning Jr, L. B. Harding and E. Kraka, *Supercomputer Algorithms for Reactivity, Dynamcis and Kinetics of Small Molecules*, Kluwer Academic Publishers, Dordrecht, Holland, 1989, p. 57.
149 G. A. Natanson, B. C. Garrett, T. N. Truong, T. Joseph and D. G. Truhlar, *J. Chem. Phys.*, 1991, **94**, 7875–7892.
150 C. F. Jackels, Z. Gu and D. G. Truhlar, *J. Chem. Phys.*, 1995, **102**, 3188–3201.
151 E. B. Wilson, *J. Chem. Phys.*, 1941, **9**, 76–84.
152 E. B. Wilson, J. C. Decius and P. C. Cross, *Molecular Vibrations*, McGraw-Hill, New York, 1955.
153 E. Kraka, W. Zou and Y. Tao, *Wiley Interdiscip. Rev.: Comput. Mol. Sci.*, 2020, **10**, 1480.
154 E. Kraka, M. Quintano, H. W. L. Force, J. J. Antonio and M. Freindorf, *J. Phys. Chem. A*, 2022, **126**, 8781–8900.
155 W. Zou, T. Sexton, E. Kraka, M. Freindorf and D. Cremer, *J. Chem. Theory Comput.*, 2016, **12**, 650–663.
156 Z. Konkoli and D. Cremer, *Int. J. Quantum Chem.*, 1998, **67**, 1–9.
157 Z. Konkoli, J. A. Larsson and D. Cremer, *Int. J. Quantum Chem.*, 1998, **67**, 11–27.
158 D. Cremer and J. A. Pople, *J. Am. Chem. Soc.*, 1975, **97**, 1354–1358.
159 C. S. López, O. N. Faza, M. Freindorf, E. Kraka and D. Cremer, *J. Org. Chem.*, 2015, **81**, 404–414.
160 Y. Tao, W. Zou, M. Freindorf, D. Cremer and E. Kraka, *pURVA, Computational and Theoretical Chemistry Group (CATCO)*, Southern Methodist University, Dallas, TX, USA, 2021.
161 S. Nanayakkara and E. Kraka, *Phys. Chem. Chem. Phys.*, 2019, **21**, 15007–15018.
162 E. Kraka, H. Joo and D. Cremer, *Mol. Phys.*, 2010, **108**, 2667–2685.
163 M. Freindorf, T. Sexton, E. Kraka and D. Cremer, *Theor. Chem. Acc.*, 2013, **133**, 1423.
164 T. M. Sexton, M. Freindorf, E. Kraka and D. Cremer, *J. Phys. Chem. A*, 2016, **120**, 8400–8418.
165 M. Freindorf, N. Beiranvand, A. A. A. Delgado, Y. Tao and E. Kraka, *J. Mol. Model.*, 2021, **27**, 320.
166 S. Nanayakkara, M. Freindorf, Y. Tao and E. Kraka, *J. Phys. Chem. A*, 2020, **124**, 8978–8993.
167 M. Freindorf and E. Kraka, Chemical Reactivity, *Approaches and Applications*, Elsevier, Heidelberg, 2021, vol. 2 pp. 301–347.
168 M. Z. Makós, M. Freindorf, Y. Tao and E. Kraka, *J. Org. Chem.*, 2021, **86**, 5714–5726.

 This journal is © The Royal Society of Chemistry 2023

169 M. C. Reis, C. S. López, E. Kraka, D. Cremer and O. N. Faza, *Inorg. Chem.*, 2016, **55**, 8636–8645.
170 M. Freindorf, D. Cremer and E. Kraka, *Mol. Phys.*, 2017, **116**, 611–630.
171 M. Freindorf, Y. Tao, D. Sethio, D. Cremer and E. Kraka, *Mol. Phys.*, 2018, **117**, 1172–1192.
172 M. Freindorf, Y. Tao and E. Kraka, *J. Comput. Biophys. Chem.*, 2022, **21**, 313–333.
173 M. Freindorf and E. Kraka, *Inorganics*, 2022, **10**, 234.
174 J. Wang, J. H. Marks, L. B. Tuli, A. M. Mebel, V. N. Azyazov and R. I. Kaiser, *J. Phys. Chem. A*, 2022, **126**, 9699–9708.
175 J. G. de la Concepción, I. Jiménez-Serra, J. C. Corchado, G. Molpeceres, A. Martínez-Henares, V. M. Rivilla, L. Colzi and J. Martín-Pintado, arXiv, astro-ph.GA, 2023, 42287.
176 J. G. de la Concepción, I. Jiménez-Serra, J. C. Corchado, G. Molpeceres, A. Martínez-Henares, V. M. Rivilla, L. Colzi and J. Martín-Pintado, *Astron. Astrophys.*, 2022, **658**, A150.
177 A. D. Becke, *J. Chem. Phys.*, 1993, **98**, 5648–5652.
178 C. Lee, W. Yang and R. G. Parr, *Phys. Rev. B: Condens. Matter Mater. Phys.*, 1988, **37**, 785–789.
179 A. D. McLean and G. S. Chandler, *J. Chem. Phys.*, 1980, **72**, 5639–5648.
180 R. Krishnan, J. S. Binkley, R. Seeger and A. Pople, *J. Chem. Phys.*, 1980, **72**, 650–654.
181 F. Neese, A. Hansen and D. G. Liakos, *J. Chem. Phys.*, 2009, **131**, 064103.
182 T. H. Dunning, *J. Chem. Phys.*, 1989, **90**, 1007–1023.
183 R. A. Kendall, T. H. Dunning and R. J. Harrison, *J. Chem. Phys.*, 1992, **96**, 6796–6806.
184 H. M. Senn and W. Thiel, *Angew. Chem., Int. Ed.*, 2009, **48**, 1198–1229.
185 L. W. Chung, W. M. C. Sameera, R. Ramozzi, A. J. Page, M. Hatanaka, G. P. Petrova, T. V. Harris, X. Li, Z. Ke, F. Liu, H.-B. Li, L. Ding and K. Morokuma, *Chem. Rev.*, 2015, **115**, 5678–5796.
186 M. Robello, E. Barresi, E. Baglini, S. Salerno, S. Taliani and F. Da Settimo, *J. Med. Chem.*, 2021, **64**, 3508–3545.
187 E. Kraka and M. Freindorf, *Reference Module in Chemistry, Molecular Sciences and Chemical Engineering – Comprehensive Computational Chemistry*, Elsevier, Heidelberg, 2022, pp. 1–27.
188 H. M. Mengist, T. Dilnessa and T. Jin, *Front. Mol. Biosci.*, 2021, **9**, 622898.
189 W. Cui, K. Yang and H. Yang, *Front. Mol. Biosci.*, 2020, **7**, 616341.
190 K. Świderek and V. Moliner, *Chem. Sci.*, 2020, **11**, 10626–10630.
191 L. Zhang, D. Lin, X. Sun, U. Curth, C. Drosten, L. Sauerhering, S. Becker, K. Rox and R. Hilgenfeld, *Science*, 2020, **368**, 409–412.
192 M. A. El Hassab, M. Fares, M. K. Abdel-Hamid Amin, S. T. Al-Rashood, A. Alharbi, R. O. Eskandrani, H. M. Alkahtani and W. M. Eldehna, *Processes*, 2021, **9**, 1004.
193 L. Zhang, D. Lin, Y. Kusov, Y. Nian, Q. Ma, J. Wang, A. von Brunn, P. Leyssen, K. Lanko, J. Neyts, A. de Wilde, E. J. Snijder, H. Liu and R. Hilgenfeld, *J. Med. Chem.*, 2021, **63**, 4562–4578.
194 D. Mondal and A. Warshel, *Biochemistry*, 2020, **59**, 4601–4608.
195 B. Halford, *Chem. Eng. News*, 2020, **98**, 1–12.
196 F. Sutanto, M. Konstantinidou and A. Dömling, *RSC Med. Chem.*, 2020, **11**, 876–884.
197 A. Aljoundi, I. Bjij, A. E. Rashedy and M. E. S. Soliman, *Protein J.*, 2020, **39**, 97–105.
198 S. A. Hollingsworth and R. O. Dror, *Neuron*, 2018, **99**, 1129–1143.
199 Y. Hong Lam, Y. Abramov, R. S. Ananthula, J. M. Elward, L. R. Hilden, S. O. Nilsson Lill, P.-O. Norrby, A. Ramirez, E. C. Sherer, J. Mustakis and G. J. Tanoury, *Org. Process Res. Dev.*, 2020, **24**, 1496–1507.
200 L. M. Mihalovits, G. G. Ferenczy and G. M. Keserü, *Int. J. Quantum Chem.*, 2022, **122**, 122:e26768.
201 D. A. Case, I. Y. Ben-Shalom, S. R. Brozell, D. S. Cerutti, T. E. Cheatham, V. W. D. Cruzeiro, T. A. Darden, R. E. Duke, D. Ghoreishi, M. K. Gilson, H. Gohlke, A. W. Goetz, D. Greene, R. Harris, N. Homeyer, S. Izadi, A. Kovalenko, T. Kurtzman, T. S. Lee, S. LeGrand, P. Li, C. Lin, J. Liu, T. Luchko, R. Luo, D. J. Mermelstein, K. M. Merz, Y. Miao, G. Monard, C. Nguyen, H. Nguyen, I. Omelyan, A. Onufriev, F. Pan, R. Qi, D. R. Roe, A. Roitberg, C. Sagui, S. Schott-Verdugo, J. Shen, C. L. Simmerling, J. Smith, R. Salomon-Ferrer, J. Swails, R. C. Walker, J. Wang, H. Wei, R. M. Wolf, X. Wu, L. Xiao, D. M. York and P. A. Kollman, *AMBER*, University of California, San Francisco, 2018.
202 L. P. Silva, I. F. S. Marra and G. W. Amarante, *Quim. Nova*, 2022, **45**, 712–727.
203 J. Fairoosa, S. Shamna and G. Anilkumar, *Appl. Organomet. Chem.*, 2021, **35**, e6356.
204 H. Zhang, X. Su and K. Dong, *Org. Biomol. Chem.*, 2020, **18**, 391–399.
205 L. Wang, Y. Shao and J. Cheng, *Org. Biomol. Chem.*, 2021, **19**, 8646–8655.
206 R. I. Patel, S. Sharma and A. Sharma, *Org. Chem. Front.*, 2021, **12**, 3166–3200.
207 S. Das, J. Maity and T. K. Panda, *Chem. Rec.*, 2022, **22**, e202200192.
208 Y. Monguchi, *Science*, 2022, **376**, 1382–1383.
209 M. S. Ahmad, I. N. Pulidindi and C. Li, *New J. Chem.*, 2020, **44**, 17177–17197.
210 K. W. Rosenmund and E. Struck, *Chem. Ber.*, 1919, **52**, 1749–1756.
211 J. F. Young, J. A. Osborn, F. H. Jardine and G. Wilkinson, *Chem. Commun.*, 1965, 131–132.
212 J. Halpern and C. S. Wong, *J. Chem. Soc., Chem. Commun.*, 1973, 629–630.
213 P. K. Soumya, T. B. Vaishak, S. Saranya and G. Anilkumar, *Appl. Organomet. Chem.*, 2021, **35**, e6340.
214 T. Aneeja, C. M. A. Afsina, P. V. Saranya and G. Anilkumar, *Beilstein J. Org. Chem.*, 2022, **128**, 37–52.
215 K. Wang, J. Zhang, R. Hu, C. Liu, T. A. Bartholome, H. Ge and B. Li, *ACS Catal.*, 2022, **12**, 2796–2820.
216 T. Katagiri and Y. Amao, *Green Chem.*, 2020, **22**, 6682–6713.
217 A. Vasseur and I. Marek, *Nat. Protoc.*, 2017, **12**, 74–87.
218 R. Martinez, M.-O. Simon, R. Chevalier, C. Pautigny, J.-P. Genet and S. Darses, *J. Am. Chem. Soc.*, 2009, **131**, 7887–7895.
219 F. Kakiuchi and T. Kochi, *Synthesis*, 2008, 3031–3039.
220 M. Torrent, M. Solà and G. Frenking, *Chem. Rev.*, 2000, **100**, 439–494.
221 C.-J. Li, *Can. J. Chem.*, 2021, **100**, 98–103.
222 A. Dhakshinamoorthy, A. M. Asiri and H. Garcia, *ACS Catal.*, 2019, **9**, 1081–1102.
223 N. G. Schmidt, E. Eger and W. Kroutil, *ACS Catal.*, 2016, **6**, 4286–4311.
224 S. K. Bera, R. Bhanja and P. Mal, *Synthesis*, 2023, **55**, 1467–1486.
225 P. B. Arockiam, C. Bruneau and P. H. Dixneuf, *Chem. Rev.*, 2012, **112**, 5879–5918.
226 J. A. Labinger and J. E. Bercaw, *Nature*, 2002, **417**, 507–514.
227 E. Jie Jack Li, *C–H Bond Activation in Organic Chemistry*, CrC Press, Boca Raton, 2015.
228 A. Kasera, J. P. Biswas, A. A. Alshehri, S. A. Al-Thabaiti, M. Mokhtar and D. Maiti, *Coord. Chem. Rev.*, 2023, **475**, 214915.
229 M. E. Evans, T. Li and W. D. Jones, *J. Am. Chem. Soc.*, 2010, **132**, 16278–16284.
230 D. Andrae, U. Häußermann, M. Dolg, H. Stoll and H. Preuß, *Theor. Chim. Acta*, 1990, **77**, 123–141.